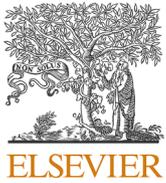# A damage-based sectional constitutive model for beams: Application to one-way textile-reinforced concrete slabs

(article starts on next page)

A damage-based sectional constitutive model for beams: Application to one-way textile-reinforced concrete slabs

Gabriel Edefors [a,b,*] , Fredrik Larsson [b], Karin Lundgren [a]

[a] Department of Architecture and Civil Engineering, Chalmers University of Technology, Gothenburg, 41258, Sweden
[b] Department of Industrial and Materials Science, Chalmers University of Technology, Gothenburg, 41258, Sweden

HIGHLIGHTS

- Thermodynamically consistent constitutive model at the cross-sectional level.
- Fully coupled membrane–bending response under cyclic and non-proportional loading.
- Captures stiffness degradation in both tension and compression.
- Calibrated using synthetic data from representative volume element simulations.
- Achieves up to two orders of magnitude speed-up over fully resolved models.

GRAPHICAL ABSTRACT
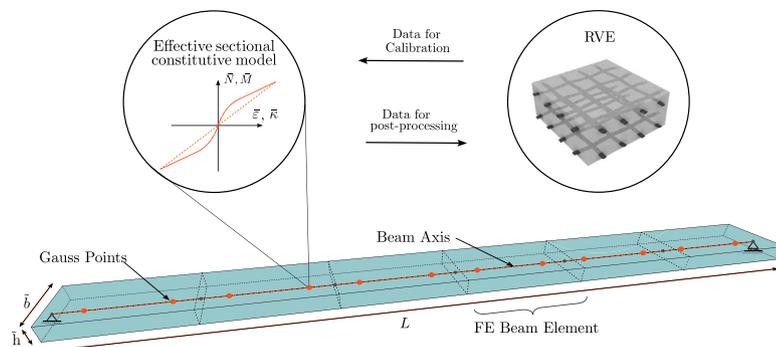
ARTICLE INFO

ABSTRACT

Accurate modeling of structures exhibiting nonlinear response due to progressive damage, such as cracking, remains a major challenge, as resolving the subscale leads to computationally intensive simulations. To address this, we propose an effective constitutive damage model formulated directly at the sectional level. By expressing the response in terms of generalized sectional quantities, the model eliminates the need for through-thickness integration and evaluation of local material behavior, improving computational efficiency. The formulation is thermodynamically consistent, employs global damage variables in the cross-section, and accounts for the coupling between normal force and bending moment. Calibration and validation are performed against representative volume element-based simulations of textile-reinforced concrete that resolve yarn–matrix slip and matrix softening. Despite its simplicity, the model accurately reproduces axial force and bending moment responses under non-proportional strain and curvature histories. Compared with a fully resolved simulation of a one-way textile-reinforced concrete slab, the model achieves a two-order-of-magnitude reduction in computational cost, with an error below 5 %. The framework captures nonlinear behavior arising from stiffness degradation, making it suitable for textile-reinforced concrete structures in which the structural response is governed by concrete cracking and crushing, as well as bond-degradation. It is, however, also applicable to other beam-like structures exhibiting damage-dominated behavior.

* Corresponding author at: Department of Architecture and Civil Engineering, Chalmers University of Technology, Gothenburg, 41258, Sweden.
  Email address: gabriel.edefors@chalmers.se (G. Edefors).

1. Introduction

Accurate modeling of heterogeneous materials such as reinforced composites remains a major challenge, as their nonlinear behavior often originates from progressive damage mechanisms acting at length scales much smaller than that of the structure. Explicitly resolving these small-scale mechanisms is computationally expensive and typically impractical at the structural level [1,2]. This motivates the development of constitutive models formulated at the cross section level, expressed in terms of generalized (resultant) stresses and strains. Such models may be phenomenological, directly calibrated from experiments, or derived from first principles via sectional analysis or homogenization of the subscale response.

Textile-reinforced concrete (TRC) provides a representative case for which this type of model is essential. TRC offers a material-efficient and corrosion-resistant alternative to conventional reinforced concrete (RC) by replacing steel bars with textile reinforcements made of carbon or glass fibers [3]. However, TRC cannot rely on the classical plasticity-based design theories used for RC, as the reinforcement materials typically exhibit brittle behavior. While plasticity theory allows RC structures to be designed based on the plastic upper bound of their capacity without explicitly modeling the progressive stress redistribution, TRC requires explicit representation of cracking, bond slip, and damage evolution to achieve reliable predictions of the ultimate-limit-state capacity [4].

Several modeling strategies have been proposed to address these challenges. For shell structures, a common approach is to discretize the cross-section into lamellae and assign distinct material behavior to each, often referred to as layered models. In phenomenological layered models, such as those proposed by El Kadi et al. [5], the lamellae are calibrated directly from experimental stress–strain data. Alternatively, layered models using a microplane formulation, first introduced for reinforced concrete (RC) shells by Wang et al. [6] and later extended to textile-reinforced concrete (TRC) by Chudoba et al. [7,8], project the macroscopic strain and stress tensors onto multiple microplanes, where the constitutive damage laws are evaluated. This approach provides a physically motivated representation of strain hardening arising from distributed cracking and bond-slip mechanisms.

More recently, computational homogenization techniques have been used to derive effective cross section responses of TRC plates and shells subjected to combined membrane and bending actions [9]. These methods use representative volume elements (RVEs) that resolve subscale features and yield homogenized section forces and moments for prescribed large-scale strains and curvatures. As a result, concurrent analysis on the large (structural) scale and the resolved subscale can be carried out, a procedure often denoted Finite Element Square FE^2 when implemented in a finite element setting. Although such FE^2 frameworks significantly reduce costs compared to fully resolved analyses, they remain computationally expensive for practical design applications [10]. In this work, two modeling scales are considered. The subscale refers to the length scale at which the reinforcement and the matrix are represented as distinct but homogeneous materials, whereas the large scale corresponds to the length scale at which the overall structure is modeled.

To reduce the computational cost of multiscale analyses while retaining the underlying physical fidelity, surrogate models have been introduced. Neural network–based surrogates show great promise [11,12], yet concerns remain regarding generalization, physical consistency, and robustness outside the training domain. Deterministic surrogate models derived from first principles therefore remain an attractive alternative when physical interpretability and robustness are required. Early examples of such models for reinforced concrete include Ibrahimbegovic et al. [13], who approximated the moment–curvature response using piecewise linear relations, and Addessi et al. [14], who proposed an uncoupled membrane–bending formulation. The Global Reinforced Concrete (GLRC) model [15,16] captures cracking-induced damage and reinforcement yielding and represents an important step toward sectional damage

modeling, but remains primarily suited for bending-dominated problems and employs simplified damage formulations that do not fully capture membrane-related damage or compressive degradation.

Reduced-order approaches derived from closed-form multiscale formulations have also been proposed. For example, Huguet et al. [17] derived an effective sectional response using a closed-form multiscale formulation based on analytical homogenization of concrete struts between cracks combined with a traction–separation law for crack behavior. While this approach provides a detailed representation of membrane-dominated response, it does not address bending behavior.

This motivates the need for a new class of sectional formulations that can efficiently act as surrogates to computational homogenization in structural-scale analyses, while preserving thermodynamic consistency and fully coupled membrane–bending behavior.

In this work, we pursue one such approach by (i) developing a computationally efficient sectional constitutive model and (ii) calibrating it to serve as a surrogate for the computationally demanding two-scale model derived through computational homogenization in [9]. The proposed sectional model is obtained by adapting and extending the global sectional formulation of [15], originally developed for plates, to beam elements, while incorporating both tensile and compressive damage under combined membrane and bending loading. The model is formulated within a thermodynamically consistent framework based on a degraded free-energy potential and four global damage variables. The formulation is specifically intended for slender, one-way TRC members subjected to combined membrane and bending loading. The numerical validation is restricted to beam cross sections with symmetric textile reinforcement layouts typical of such structures. The fully coupled treatment of membrane and bending actions enables the simulation of asymmetric damage states and the response of structures subjected to significant axial forces, such as curved one-way slabs and beams. The RVE modeling approach has been experimentally validated in previous work [18], and the homogenization framework has been validated numerically in [9]. Accordingly, the validation in this work concerns the accuracy of the proposed model as a reduced-order surrogate of the computational homogenization model. The surrogate model is calibrated and validated using multiple sets of RVE simulation data for TRC beams, and its predictive capability is demonstrated through a case study of a cyclically loaded one-way slab with fixed ends.

2. Modeling framework: sectional constitutive model

This chapter begins with a brief overview of the proposed model and its associated workflow. The constitutive model for the effective beam cross section is then derived in Section 2.2, including a closed-form solution strategy for uniform rectangular members. Finally, a calibration procedure for the effective model based on representative volume element (RVE) simulations of TRC is presented in Section 2.3.

2.1. Model overview

The proposed sectional constitutive model operates at the level of the beam cross section and can be employed in both analytical and numerical beam formulations. As illustrated in Fig. 1, the framework comprises two stages: an offline calibration stage, in which the constitutive parameters are identified from synthetic data obtained from representative volume element simulations of the resolved subscale response; and an online simulation stage, in which the calibrated constitutive model is evaluated at each integration point of an effective finite element beam model.

Within this framework, the sectional constitutive model acts as a local operator mapping generalized kinematics to stress resultants. The kinematic inputs are the generalized axial strain and curvature, while the outputs are the normal force and bending moment. The internal state variables comprise (i) driving variables defined by the maximum attained strain-energy release rates and (ii) tensile and compressive
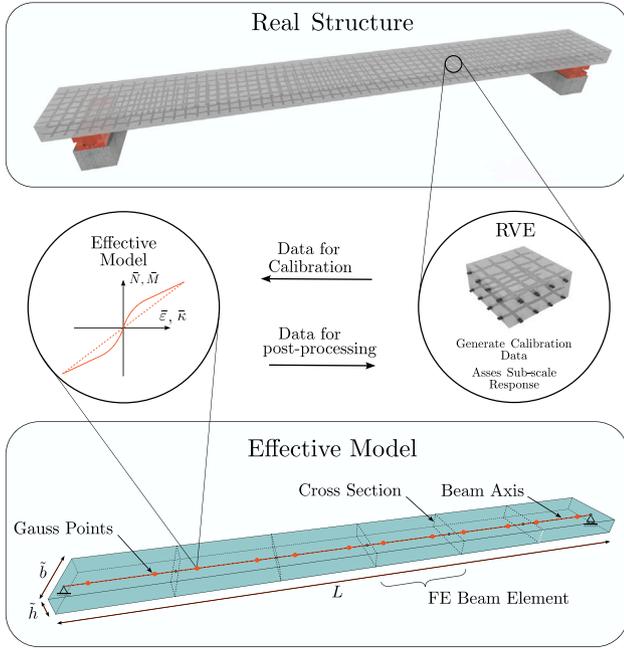
Fig. 1. Illustration of the relation between a real-world structure, in this case a textile-reinforced beam, and an effective FE beam model. In the proposed workflow, the RVE acts as a virtual laboratory to produce calibration data for the surrogate model. The model is then used as constitutive driver at Gauss-point level of the effective beam model. It is also possible to go back to the RVE at a certain state and asses the subscale response as indicated by the arrow going from left to right.

damage variables for the upper and lower parts of the cross section; four damage variables are used. The internal states are updated incrementally via an explicit evolution law. Furthermore, the formulation is based on a generalized free-energy potential, from which the normal force and bending moment follow as energy-conjugate quantities to the kinematic variables.

2.2. Derivation of the sectional constitutive model

The idea of the (effective) sectional model is to approximate the response of a generic, possibly composite, cross section with a simplified equivalent one characterized by a reduced set of parameters, see Fig. 2. In this context, the term *effective* refers to a model that approximates the sectional response of the underlying detailed model. To derive the effective model directly at the sectional level, the three-dimensional strain and stress fields are reduced by expressing them in terms of a limited set of generalized sectional quantities.

Fig. 2 illustrates the underlying modeling assumption of the effective sectional approach, namely that the detailed three-dimensional stress and damage state associated with a given generalized strain can be represented, at the sectional level, by energetically equivalent generalized stress resultants and a small set of global damage variables, in line with the conceptual framework originally proposed by Koechlin et al. [15].

2.2.1. Generalized quantities of the beam section

Consider a beam cross section subjected to combined axial and bending actions. Under the Euler–Bernoulli assumption, the strain distribution in the cross section can be described by only two generalized strain measures: the average axial strain $\bar{\varepsilon}$ and the curvature $\bar{\kappa}$ [19]. Accordingly, the through-thickness strain field is expressed as

$$\varepsilon(z) = \bar{\varepsilon} - z\,\bar{\kappa}, \tag{1}$$

where z denotes the coordinate in the transverse direction of the cross section (cf. Fig. 2). The chosen sign convention implies that a positive
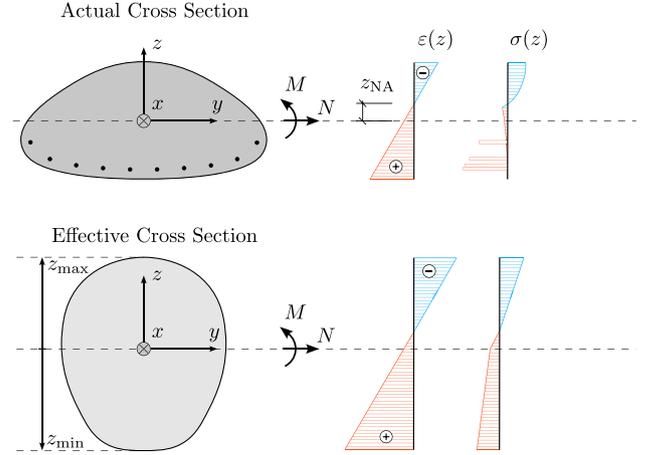
Fig. 2. Comparison of a heterogeneous cross section with an equivalent effective cross section, illustrating the corresponding strain and stress distributions. The coordinate system is indicated in the figure. z_{NA} denotes the distance from the midplane to the kinematic neutral axis.

curvature results in compression at the top and tension at the bottom of the beam. We also postulate the existence of a stress function $\sigma(\varepsilon(z))$ that depends on the strain in Eq. (1), and possibly on a set of internal variables. From the current choice of the generalized kinematic variables, it is possible to write the virtual work of the beam section as

$$\delta W_{\mathrm{int}} = \delta\bar{\varepsilon}\int_A \sigma(\varepsilon(z))\,\mathrm{d}A, -\delta\bar{\kappa}\int_A z\,\sigma(\varepsilon(z))\,\mathrm{d}A. \tag{2}$$

From this expression, the generalized stress resultants can be identified as $\bar{N}$, conjugate to the generalized strain $\bar{\varepsilon}$, and $\bar{M}$, conjugate to $\bar{\kappa}$. In this setting, $\bar{N}$ represents the normal force and $\bar{M}$ the bending moment, defined as

$$\bar{N} = \int_A \sigma(\varepsilon(z))\,\mathrm{d}A, \qquad \bar{M} = -\int_A z\sigma(\varepsilon(z))\,\mathrm{d}A. \tag{3}$$

2.2.2. Linear elastic response

Following the approach of Koechlin et al. [15], the generalized free energy density $\bar{\Psi}^0$ of the effective section is obtained by integrating the local free energy density

$$\Psi^0(\varepsilon; z) = \frac{1}{2}C(z)\varepsilon^2 \tag{4}$$

over the cross section using Eq. (1), yielding

$$\bar{\Psi}^0(\bar{\varepsilon}, \bar{\kappa}) = \frac{1}{2}\int_A \Psi^0(\varepsilon; z)\,\mathrm{d}A = \frac{1}{2}\int_A C(z)\left(\bar{\varepsilon} - z\bar{\kappa}\right)^2\,\mathrm{d}A. \tag{5}$$

Here, $C(z)$ denotes the stiffness parameter, which may vary along the section height. Since torsional effects are not considered, it is sufficient to account for variation with respect to z only, while neglecting any variation in y. Expanding the square leads to the quadratic form

$$\bar{\Psi}^0(\bar{\varepsilon}, \bar{\kappa}) = \frac{\bar{C}_A^0\bar{\varepsilon}^2}{2} - \bar{C}_S^0\bar{\varepsilon}\bar{\kappa} + \frac{\bar{C}_I^0\bar{\kappa}^2}{2}, \tag{6}$$

where the membrane, coupling, and bending contributions are $\bar{\Psi}_m^0 = \frac{1}{2}\bar{C}_A^0\bar{\varepsilon}^2$, $\bar{\Psi}_{m,b}^0 = -\bar{C}_S^0\bar{\varepsilon}\bar{\kappa}$, and $\bar{\Psi}_b^0 = \frac{1}{2}\bar{C}_I^0\bar{\kappa}^2$, respectively. The generalized sectional stiffness coefficients are defined as

$$\bar{C}_A^0 = \int_A C(z)\,\mathrm{d}A, \qquad \bar{C}_S^0 = \int_A C(z)\,z\,\mathrm{d}A, \qquad \bar{C}_I^0 = \int_A C(z)\,z^2\,\mathrm{d}A. \tag{7}$$

These are the coefficients that represent the effective stiffness in the model and must therefore be calibrated within the surrogate modeling framework.

We are now in the position to derive the expressions for the generalized stress variables by differentiating the free energy with respect to the generalized strain variables

$$\bar{N}^0 = \frac{\partial \bar{\Psi}^0}{\partial \bar{\varepsilon}} = \frac{\partial \bar{\Psi}_{\mathrm{m}}^0}{\partial \bar{\varepsilon}} + \frac{\partial \bar{\Psi}_{\mathrm{m,b}}^0}{\partial \bar{\varepsilon}} = \bar{C}_{\mathrm{A}}^0 \bar{\varepsilon} - \bar{C}_{\mathrm{S}}^0 \bar{\kappa}, \tag{8a}$$

$$\bar{M}^0 = \frac{\partial \bar{\Psi}^0}{\partial \bar{\kappa}} = \frac{\partial \bar{\Psi}_{\mathrm{b}}^0}{\partial \bar{\kappa}} + \frac{\partial \bar{\Psi}_{\mathrm{m,b}}^0}{\partial \bar{\kappa}} = \bar{C}_{\mathrm{I}}^0 \bar{\kappa} - \bar{C}_{\mathrm{S}}^0 \bar{\varepsilon}, \tag{8b}$$

The familiar expressions for the normal force and the bending moment in Eq. (8) are the same as those that can be found in the literature for a general linear elastic cross section, e.g., in [20]. In the linear elastic setting, the problem can always be decoupled by placing the coordinate system in the stiffness centroid, such that $\bar{C}_{\mathrm{S}}^0$ in Eq. (7) vanishes.

Remark 1. At this stage we have made no assumption about the geometry or stiffness distribution of the effective (fictitious) cross section. Consequently, the integrated quantities in Eq. (7) can be treated as model parameters and can be calibrated directly without any notion of the distribution of area and stiffness.

Remark 2. The sectional stiffness coefficient $C(z)$ may be interpreted differently depending on the assumed kinematic constraints. For a beam, i.e., under the constraint $\sigma_{yy} = 0$ and $\sigma_{zz} = 0$, $C(z)$ represents the Young's modulus of the effective section. For a transversely constrained one-way slab, where $\varepsilon_{yy} = 0$ and $\sigma_{zz} = 0$, the effective stiffness becomes $C(z) = E(z)/(1 - \nu(z)^2)$, where $E(z)$ is the Young's modulus and $\nu(z)$ is the Poisson ratio of each position z. The latter expression can thus be interpreted as a scaling of the Young's modulus accounting for the Poisson effect. Importantly, both cases are represented by a single scalar stiffness parameter $C(z)$, such that the formal structure of the constitutive model remains unchanged.

2.2.3. Accounting for damage

We now extend the model to account for damage. To this end, we introduce the tensile damage variables $d_{\mathrm{u}}^{\mathrm{t}} \geq 0$ and $d_{\mathrm{l}}^{\mathrm{t}} \geq 0$, associated with the upper and lower parts of the cross section, respectively, following the approach in [15]. In an analogous manner, the compressive damage variables $d_{\mathrm{u}}^{\mathrm{c}} \geq 0$ and $d_{\mathrm{l}}^{\mathrm{c}} \geq 0$ are defined for the upper and lower parts of the cross section, respectively. The four damage variables are collected in the set $\bar{d} = (d_{\mathrm{u}}^{\mathrm{t}}, d_{\mathrm{l}}^{\mathrm{t}}, d_{\mathrm{u}}^{\mathrm{c}}, d_{\mathrm{l}}^{\mathrm{c}})$. The precise definition of the upper and lower regions will be specified later. As in the linear elastic case, the degraded generalized free energy density $\bar{\Psi}$ of the effective section is obtained by integrating the degraded free energy density over the cross section.

Now, if we define the upper part as $z \in [0, z_{\mathrm{max}}]$ and the lower part as $z \in [z_{\mathrm{min}}, 0)$, we can introduce the damage activation functions as

$$d^{\mathrm{t}}(z) = \begin{cases} d_{\mathrm{u}}^{\mathrm{t}}, & z \in [0, z_{\mathrm{max}}], \\ d_{\mathrm{l}}^{\mathrm{t}}, & z \in [z_{\mathrm{min}}, 0), \end{cases} \tag{9}$$

$$d^{\mathrm{c}}(z) = \begin{cases} d_{\mathrm{u}}^{\mathrm{c}}, & z \in [0, z_{\mathrm{max}}], \\ d_{\mathrm{l}}^{\mathrm{c}}, & z \in [z_{\mathrm{min}}, 0), \end{cases} \tag{10}$$

As for the linear elastic case, the generalized free energy density $\bar{\Psi}$ of the effective section is obtained by integrating the degraded free energy density over the cross section.

$$\bar{\Psi}(\bar{\varepsilon}, \bar{\kappa}, \bar{d}) = \int_A \Psi(\bar{\varepsilon} - z\,\bar{\kappa}, \bar{d}; z)\,\mathrm{d}A, \tag{11}$$

where the local degraded free energy density is defined as

$$\Psi(\varepsilon, \bar{d}; z) = \frac{C(z)}{2} \left[(1 - d^{\mathrm{t}}(z)) \langle \varepsilon(z) \rangle_+^2 + (1 - d^{\mathrm{c}}(z)) \langle \varepsilon(z) \rangle_-^2 \right]. \tag{12}$$

For brevity, we may also introduce the damage activation function[1]

---

[1] Here, $H(\cdot)$ denotes the Heaviside step function.

$$\zeta(\bar{\varepsilon}, \bar{\kappa}, \bar{d}; z) = (1 - d^{\mathrm{t}}(z))\,H(\bar{\varepsilon} - z\bar{\kappa}) + (1 - d^{\mathrm{c}}(z))\,H(-(\bar{\varepsilon} - z\bar{\kappa})).$$

such that the generalized free energy density can be expressed as an integration over the whole cross section,

$$\bar{\Psi}(\bar{\varepsilon}, \bar{\kappa}, \bar{d}) = \int_A \zeta(\bar{\varepsilon}, \bar{\kappa}, \bar{d}; z)\,\Psi^0\,\mathrm{d}A = \frac{1}{2} \int_A \zeta(\bar{\varepsilon}, \bar{\kappa}, \bar{d}; z)\,C(z)\,[\bar{\varepsilon} - z\bar{\kappa}]^2\,\mathrm{d}A. \tag{13}$$

Once again, by expanding the square, it is possible to write

$$\bar{\Psi}(\bar{\varepsilon}, \bar{\kappa}, \bar{d}) = \tfrac{1}{2}\bar{C}_{\mathrm{A}}(\bar{\varepsilon}, \bar{\kappa}, \bar{d})\bar{\varepsilon}^2 - \bar{C}_{\mathrm{S}}(\bar{\varepsilon}, \bar{\kappa}, \bar{d})\bar{\varepsilon}\bar{\kappa} + \tfrac{1}{2}\bar{C}_{\mathrm{I}}(\bar{\varepsilon}, \bar{\kappa}, \bar{d})\bar{\kappa}^2 = \bar{\Psi}_{\mathrm{m}} + \bar{\Psi}_{\mathrm{m,b}} + \bar{\Psi}_{\mathrm{b}}, \tag{14}$$

where the degraded generalized stiffness coefficients are defined as

$$\bar{C}_{\mathrm{A}}(\bar{\varepsilon}, \bar{\kappa}, \bar{d}) := \int_A C(z)\,\zeta(\bar{\varepsilon}, \bar{\kappa}, \bar{d}; z)\,\mathrm{d}A, \tag{15a}$$

$$\bar{C}_{\mathrm{S}}(\bar{\varepsilon}, \bar{\kappa}, \bar{d}) := \int_A C(z)\,z\,\zeta(\bar{\varepsilon}, \bar{\kappa}, \bar{d}; z)\,\mathrm{d}A, \tag{15b}$$

$$\bar{C}_{\mathrm{I}}(\bar{\varepsilon}, \bar{\kappa}, \bar{d}) := \int_A C(z)\,z^2\,\zeta(\bar{\varepsilon}, \bar{\kappa}, \bar{d}; z)\,\mathrm{d}A. \tag{15c}$$

The expressions for the degraded generalized stresses are once again obtained by differentiating the free energy density,

$$\bar{N} = \left.\frac{\partial \bar{\Psi}}{\partial \bar{\varepsilon}}\right|_{\bar{\kappa}, \bar{d}} = \bar{C}_{\mathrm{A}}(\bar{\varepsilon}, \bar{\kappa}, \bar{d})\bar{\varepsilon} - \bar{C}_{\mathrm{S}}(\bar{\varepsilon}, \bar{\kappa}, \bar{d})\bar{\kappa}, \tag{16a}$$

$$\bar{M} = \left.\frac{\partial \bar{\Psi}}{\partial \bar{\kappa}}\right|_{\bar{\varepsilon}, \bar{d}} = \bar{C}_{\mathrm{I}}(\bar{\varepsilon}, \bar{\kappa}, \bar{d})\bar{\kappa} - \bar{C}_{\mathrm{S}}(\bar{\varepsilon}, \bar{\kappa}, \bar{d})\bar{\varepsilon}. \tag{16b}$$

See Appendix A for details of the derivation and a complete discussion of the regions where the damage activation function changes value. Similarly, the strain energy release rates, i.e., the conjugate variables to the damage variables, are evaluated as

$$Y_{\mathrm{u}}^{\mathrm{t/c}}(\bar{\varepsilon}, \bar{\kappa}) = -\left.\frac{\partial \bar{\Psi}}{\partial d_{\mathrm{u}}^{\mathrm{t/c}}}\right|_{\bar{\varepsilon}, \bar{\kappa}} = \frac{1}{2} \int_{A_{\mathrm{u}}} C(z) \left\langle \bar{\varepsilon} - z\bar{\kappa} \right\rangle_\pm^2 \,\mathrm{d}A, \tag{17a}$$

$$Y_{\mathrm{l}}^{\mathrm{t/c}}(\bar{\varepsilon}, \bar{\kappa}) = -\left.\frac{\partial \bar{\Psi}}{\partial d_{\mathrm{l}}^{\mathrm{t/c}}}\right|_{\bar{\varepsilon}, \bar{\kappa}} = \frac{1}{2} \int_{A_{\mathrm{l}}} C(z) \left\langle \bar{\varepsilon} - z\bar{\kappa} \right\rangle_\pm^2 \,\mathrm{d}A. \tag{17b}$$

See Appendix C for more details.

2.2.4. Damage evolution

Within the standard framework of continuum damage mechanics, we introduce loading functions for tension/compression in the upper/lower part of the cross section, ($\phi_{\mathrm{u}}^{\mathrm{t}}$, $\phi_{\mathrm{l}}^{\mathrm{t}}$, $\phi_{\mathrm{u}}^{\mathrm{c}}$, and $\phi_{\mathrm{l}}^{\mathrm{c}}$), defined in terms of the strain-energy release rates introduced in Eq. (17a), following the formulations of Koechlin et al. [15] and Marigo [21]. These functions serve to identify the activation of damage and to ensure consistent damage evolution.

$$\phi_{\mathrm{u}}^{\mathrm{t/c}} = Y_{\mathrm{u}}^{\mathrm{t/c}}(\bar{\varepsilon}, \bar{\kappa}, d_{\mathrm{u}}^{\mathrm{t/c}}) - k_{\mathrm{u}}^{\mathrm{t/c}}, \qquad \phi_{\mathrm{l}}^{\mathrm{t/c}} = Y_{\mathrm{l}}^{\mathrm{t/c}}(\bar{\varepsilon}, \bar{\kappa}, d_{\mathrm{l}}^{\mathrm{t/c}}) - k_{\mathrm{l}}^{\mathrm{t/c}}. \tag{18a}$$

The parameters $k_{\mathrm{u}}^{\mathrm{t}}$ and $k_{\mathrm{u}}^{\mathrm{c}}$ define the strain energy release rates at the onset of tensile and compressive damage in the upper part of the beam, respectively. Similarly, $k_{\mathrm{l}}^{\mathrm{t}}$ and $k_{\mathrm{l}}^{\mathrm{c}}$ define the corresponding values for the lower part. These parameters are treated as model parameters that must be calibrated.

Remark 3. An immediate consequence of using the strain-energy release rate as the damage-driving variable is that crack initiation does not correspond to a unique maximum strain. For instance, comparing pure membrane strain $\varepsilon(z) = \bar{\varepsilon}$ and pure bending $\varepsilon(z) = -z\bar{\kappa}$ with the
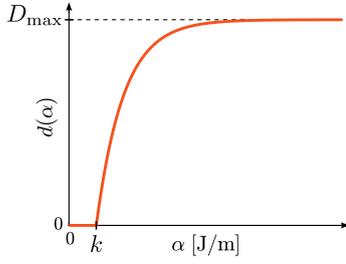
Fig. 3. Schematic graph of the damage evolution function illustrating the threshold k and the upper cap $D_{\max}$.

same outer-fiber strain $\varepsilon_{\max}$, one obtains $Y_l^m = 3Y_l^b$. Hence, the onset of damage depends on the deformation mode rather than on a single strain value.

At this point there are at least two different ways to define the damage evolution. Either we could implicitly solve for the damage variables using the KKT conditions as in [15], or we could define an explicit damage evolution law. In this work the latter approach will be used, since it allows for a richer parameter space and a greater possibility to calibrate the model. To this end we introduce the internal variables $\alpha_u^t, \alpha_u^c, \alpha_l^t$ and α_l^c, defined as the maximum attained strain energy release rates, i.e.,

$$\alpha_u^{t/c}(t) = \max_{\tau \in [0,t]} \left(Y_u^{t/c}(\tau)\right), \qquad \alpha_l^{t/c}(t) = \max_{\tau \in [0,t]} \left(Y_l^{t/c}(\tau)\right), \tag{19}$$

ensuring that the irreversibility condition is fulfilled. Inspired by Mazars [22], we then adopt an exponential evolution law for all damage variables, expressed in terms of these internal variables:

$$d(\alpha; k, \beta, D_{\max}) = \begin{cases} 0, & \alpha < k, \\ D_{\max}\left[1 - \exp\left(-\frac{\alpha - k}{\beta}\right)\right], & \alpha \geq k, \end{cases} \tag{20}$$

where $D_{\max} \in [0,1]$ limits the damage to a value smaller than 1 (Fig. 3).

2.2.5. Model consistency

To ensure model consistency, the formulation must satisfy the second law of thermodynamics and fulfill the condition of thermodynamic stability [23,24]. The first requirement is satisfied if the model predicts non-negative energy dissipation, while stability follows from the convexity of the Helmholtz free energy with respect to the generalized strain variables, as discussed by Lubarda [24].

Energy dissipation. The requirement of non-negative energy dissipation can be formulated in terms of the Clausius–Duhem inequality,

$$D = \left(Y_u^t d_u^t + Y_u^c d_u^c\right) + \left(Y_l^t d_l^t + Y_l^c d_l^c\right) \geq 0. \tag{21}$$

From Eq. (20), it follows that $\dot{d} \geq 0$, hence it suffices to show that

$$Y_u^t \geq 0, \qquad Y_u^c \geq 0, \qquad Y_l^t \geq 0, \qquad Y_l^c \geq 0. \tag{22}$$

to fulfill Eq. (21). This inequality can easily be verified by noting that the integrands in Eq. (17a) are non-negative, hence the energy dissipation is always non-negative.

Convexity of the free energy function. The degraded free energy $\bar{\Psi}(\bar{\varepsilon}, \bar{\kappa})$ is convex in the generalized strains if its Hessian with respect to $(\bar{\varepsilon}, \bar{\kappa})$ is positive semi-definite. For the present formulation, the Hessian of the free energy can be expressed in terms of the generalized stresses as

$$H = \begin{bmatrix} \dfrac{\partial^2 \bar{\Psi}}{\partial \bar{\varepsilon}^2} & \dfrac{\partial^2 \bar{\Psi}}{\partial \bar{\varepsilon}\,\partial \bar{\kappa}} \\ \dfrac{\partial^2 \bar{\Psi}}{\partial \bar{\kappa}\,\partial \bar{\varepsilon}} & \dfrac{\partial^2 \bar{\Psi}}{\partial \bar{\kappa}^2} \end{bmatrix} = \begin{bmatrix} \dfrac{\partial \bar{N}}{\partial \bar{\varepsilon}} & \dfrac{\partial \bar{N}}{\partial \bar{\kappa}} \\ \dfrac{\partial \bar{M}}{\partial \bar{\varepsilon}} & \dfrac{\partial \bar{M}}{\partial \bar{\kappa}} \end{bmatrix} = \begin{bmatrix} \bar{C}_A & -\bar{C}_S \\ -\bar{C}_S & \bar{C}_I \end{bmatrix}, \tag{23}$$

except at $\bar{\varepsilon} = \bar{\kappa} = 0$, where H is undefined, whenever $d_u^t \neq d_u^c$ or $d_l^t \neq d_l^c$. The detailed derivation of the first component $\partial \bar{N}/\partial \bar{\varepsilon} = \bar{C}_A$ is provided in Appendix B, while the remaining terms follow by direct analogy.

For H to be positive semi-definite, we require that

$$H_{11} = \bar{C}_A \geq 0, \tag{24a}$$

$$\det(H) = \bar{C}_A \bar{C}_I - \bar{C}_S^2 \geq 0. \tag{24b}$$

The first condition in Eq. (24a) is trivially satisfied from the definition in Eq. (15). By inserting the definitions of $\bar{C}_A$, $\bar{C}_S$ and $\bar{C}_I$ from Eq. (15), the inequality in Eq. (24b) can be written as

$$\left(\int_A C(z)z\zeta(z)\,\mathrm{d}A\right)^2 \leq \int_A C(z)\zeta(z)\,\mathrm{d}A \int_A C(z)z^2\zeta(z)\,\mathrm{d}A. \tag{25}$$

The inequality in Eq. (25) follows from the Cauchy–Schwarz inequality, since the weighting function $C(z)\zeta(z)$ is piecewise nonnegative. Therefore, the matrix H is positive semi definite, which implies that the Helmholtz free energy is convex.

Remark 4. The Hessian H defined in Eq. (23) corresponds to the *frozen state* tangent stiffness, i.e., the response at unloading. In contrast, the *consistent* tangent stiffness, required in the Newton–Raphson iterations of the large-scale equilibrium problem is obtained as

$$H_{\mathrm{cons}} = \left.\frac{\partial \bar{\sigma}}{\partial \bar{\varepsilon}}\right|_{\bar{d}} + \sum_{i=1}^{4} \frac{\partial \bar{\sigma}}{\partial d_i} \otimes \frac{\partial d_i}{\partial \bar{\varepsilon}}, \tag{26}$$

where the generalized stress and strain vectors are defined as $\bar{\sigma} = [\bar{N}\ \bar{M}]^{\mathsf{T}}$ and $\bar{\varepsilon} = [\bar{\varepsilon}\ \bar{\kappa}]^{\mathsf{T}}$ and $\{d_i\}_{i=1}^{4}$ represents the four damage variables in $\bar{d}$.

While H is always symmetric and positive semi-definite as long as damage is frozen, the H_{cons} may lose (semi)positive definiteness during damage evolution, leading to strain-softening, and eventual loss of ellipticity associated with localization phenomena [25].

2.2.6. Closed-form solution for uniform rectangular cross sections

For the special case of a uniform rectangular cross section with constant stiffness $C(z) = C$, width $\tilde{b}$, and height $\tilde{h}$, closed-form expressions of the sectional model can be obtained. The coordinate system is placed at the centroid, such that $z_{\max} = \tilde{h}/2$ and $z_{\min} = -\tilde{h}/2$ and the height $\tilde{h}$ is treated as an adjustable model parameter, as illustrated in Fig. 4. Under these assumptions, it is possible to derive closed form solutions to the integrals in Eq. (15), thereby removing the need for numerical integration.

For any given strain distribution, the sectional integrals can be divided into three regions with constant damage, which can be evaluated analytically. However, since the neutral axis may shift from the upper to the lower part of the section (or vice versa) during loading, two auxiliary neutral axes are introduced–one for each part. This allows the integrals to be subdivided into four regions in total, as illustrated in Fig. 5. The positions of the upper and lower neutral axes are defined as

$$z_{\mathrm{NA,u}} = \begin{cases} \dfrac{\bar{\varepsilon}}{\bar{\kappa}}, & \text{if } \dfrac{\bar{\varepsilon}}{\bar{\kappa}} \geq 0 \text{ and } \left|\dfrac{\bar{\varepsilon}}{\bar{\kappa}}\right| \leq \dfrac{\tilde{h}}{2}, \\ 0, & \text{otherwise}, \end{cases} \qquad z_{\mathrm{NA,l}} = \begin{cases} \dfrac{\bar{\varepsilon}}{\bar{\kappa}}, & \text{if } \dfrac{\bar{\varepsilon}}{\bar{\kappa}} < 0 \text{ and } \left|\dfrac{\bar{\varepsilon}}{\bar{\kappa}}\right| \leq \dfrac{\tilde{h}}{2}, \\ 0, & \text{otherwise}. \end{cases} \tag{27}$$

The four integration parts are defined as follows:

1. $z > z_{\mathrm{NA,u}}$,
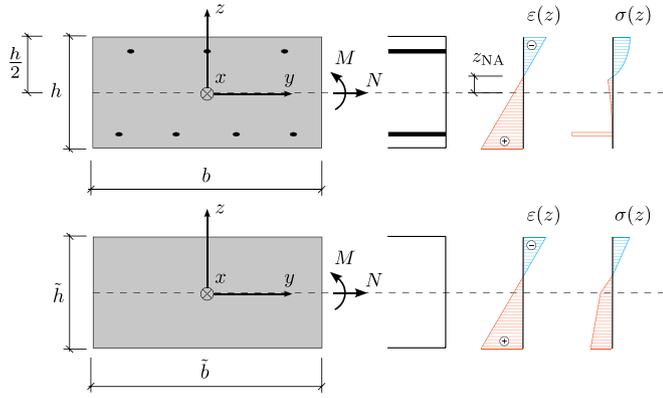2. $0 < z < z_{\mathrm{NA,u}}$,

Fig. 4. Comparison of a double reinforced TRC cross section with its equivalent effective cross section, illustrating the corresponding strain and stress distributions.

3. $z_{\mathrm{NA,l}} < z < 0$,
4. $z < z_{\mathrm{NA,l}}$.

Since the strain varies linearly through the section, it is sufficient to evaluate the damage activation function at the discrete points $z_i \in \{\tilde{h}/2, 0, 0, -\tilde{h}/2\}$, as shown in Fig. 5. If the neutral axis lies in the upper part of the section, part 3 vanishes; if it lies in the lower part, part 2 vanishes. With this partitioning, the closed-form expressions for the sectional quantities can be evaluated as

$$\bar{C}_A = C\tilde{b} \sum_{i=1}^{4} A_i\, \zeta(z_i), \quad \bar{C}_S = C\tilde{b} \sum_{i=1}^{4} S_i\, \zeta(z_i), \quad \bar{C}_I = C\tilde{b} \sum_{i=1}^{4} I_i\, \zeta(z_i). \quad (28)$$

where A_i, S_i and I_i is the area and the first and second moment of area for the different parts, see Appendix G. Similarly, the closed form solutions for for the strain energy release rates can be written as

$$Y_u^t = \frac{C\tilde{b}}{2} \sum_{i=1}^{2} H(\varepsilon(z_i))\, Q_i(\bar{\varepsilon}, \bar{\kappa}), \quad Y_u^c = \frac{C\tilde{b}}{2} \sum_{i=1}^{2} H(-\varepsilon(z_i))\, Q_i(\bar{\varepsilon}, \bar{\kappa}), \quad (29a)$$

$$Y_l^t = \frac{C\tilde{b}}{2} \sum_{i=3}^{4} H(\varepsilon(z_i))\, Q_i(\bar{\varepsilon}, \bar{\kappa}), \quad Y_l^c = \frac{C\tilde{b}}{2} \sum_{i=3}^{4} H(-\varepsilon(z_i))\, Q_i(\bar{\varepsilon}, \bar{\kappa}), \quad (29b)$$

where we have introduced the quadratic form

$$Q_i(\bar{\varepsilon}, \bar{\kappa}) := A_i \bar{\varepsilon}^2 + I_i \bar{\kappa}^2 - 2 S_i \bar{\varepsilon}\bar{\kappa}. \quad (30)$$

These expressions are then substituted in place of the expressions in Eqs. (15) and (17).

2.3. Generation of calibration and validation data from virtual testing

Synthetic data used for the calibration and validation in Section 3 are obtained from subscale RVE simulations, as outlined by Edefors et al. [9].

2.3.1. RVE model

In the RVEs, the concrete is modeled as a continuum with an isotropic damage model extended from Mazars modified model in [26]. In this model, the (apparent) stress in the concrete σ_c is expressed in terms of the effective stress $\sigma_c^0 = E_c : \varepsilon_c$ such that $\sigma_c = (1 - d)\sigma_c^0$

The degradation is described using the scalar damage variable d, which evolves according to

$$d = 1 - \frac{(1 - A)\mu_0}{\mu} - A\left(\frac{\mu_0}{\mu}\right)^r \exp\left(-B(\mu - \mu_0)\right), \quad (31)$$

where μ is the driving variable, weighted from the maximum attained tensile and compressive equivalent strains according to $\mu = r\mu_r + (1-r)\mu_c$. Here r is a variable characterizing the state of the stress (tension or compression), A and B are coefficients depending on the stress state and μ_0 is the strain threshold, see [26]. In this work, the factor $\left(\frac{\mu_0}{\mu}\right)^r$ is added to make it possible to regularize the model without overestimating the tensile strength. Also, compared to the proposed model in [26], the equivalent strain measures are defined in terms of the positive and negative parts of the strain tensor

$$\varepsilon_t = \sqrt{\sum_{i=1}^{3} \langle \varepsilon_i \rangle^2}, \qquad \varepsilon_c = \sqrt{\sum_{i=1}^{3} \langle -\varepsilon_i \rangle^2}. \quad (32)$$

Finally, the model is regularized using the crack-band method, see [27]. Consequently, the parameter B_t is chosen such that the fracture energy G_F is respected for the case of uniaxial tension for the specific choice of $A_t = 1$. Assuming that the softening localizes over crack-band width h_{cb}, it is possible to express B_t as

$$B_t = \frac{2 E \varepsilon_{t,0}\, h_{cb}}{2 G_F - E \varepsilon_{t,0}^2\, h_{cb}}. \quad (33)$$

For further details on the damage model, the reader is referred to Mazars 2015 [26].

The yarns are assumed to behave linearly elastically up to failure, with the non-uniform stress distribution accounted for by the efficiency factors η_E for the stiffness and η_f for the strength [9,28]. The yarns are modeled as one-dimensional truss elements and are assumed to carry stress only in tension, following the approach in Richter [29]. The bond–slip between yarns and matrix is described by a one-dimensional model with linear elastic unloading to account for bond degradation, calibrated against pull-out tests of TRC specimens [28].

The considered RVE has a side length of $L_\square = 50$ mm, a thickness h in the range 10 mm to 20 mm, and contains two yarns in each direction in both the top and bottom reinforcement layers. Furthermore, the RVE problem is solved incrementally for prescribed generalized strain histories in COMSOL using the finite element method, with the mesh shown in Fig. 6. In the following, strongly periodic boundary conditions are applied, meaning that the displacement jump vector is prescribed
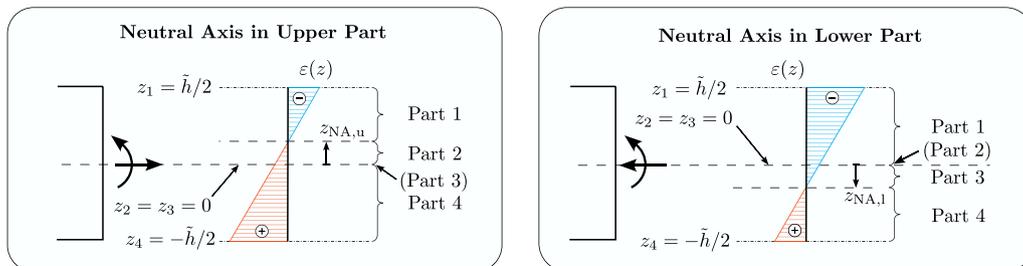

Fig. 5. Closed-form evaluation of the sectional integrals using the linear strain profile and the auxiliary neutral axes.
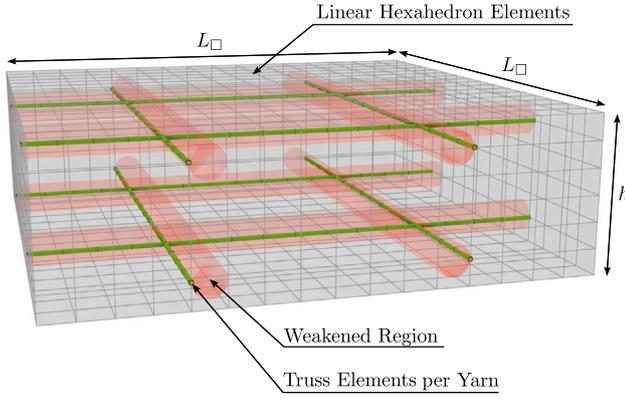
Fig. 6. Finite element discretization of the RVE problem for $h = 15\,\text{mm}$, showing the mesh of the concrete matrix and the yarns, as well as the weakened regions.

according to

$$\begin{pmatrix} [\![u_x]\!] \\ [\![u_z]\!] \end{pmatrix} = \begin{pmatrix} \bar{\varepsilon}\, L_\square - z\, \bar{\kappa}\, L_\square \\ \frac{1}{2}\, \bar{\kappa}\, L_\square^2 \end{pmatrix}, \tag{34}$$

together with suitable point constraints to suppress rigid body motion. The concrete matrix is discretized using linear hexahedral elements of size $3.125 \times 3.125 \times 2.500\,\text{mm}$, while the yarns are modeled with truss elements of length $3.125\,\text{mm}$. The element sizes are determined based on a linear convergence study. Local weakening due to the yarns is modeled by proportionally reducing the tensile strength, fracture energy, and Young's modulus of the adjacent concrete elements, see [9]. The parameters used to solve the RVE problem are presented in Appendix E.

2.3.2. Upscaling to obtain normal forces and bending moments

The generalized stresses $\bar{N}$ and $\bar{M}$ for a given combination of generalized strains $\bar{\varepsilon}$ and $\bar{\kappa}$ are obtained through variationally consistent homogenization of the response of a representative volume element (RVE). For further details, the reader is referred to Edefors [9]. In short, the RVE is subjected to prescribed generalized strain histories. The resulting generalized stress fields in the concrete and the yarns are computed from the homogenization operators on the RVE length $|L_\square|$,

$$\bar{N} = \frac{1}{|L_\square|}\left[\int_{\Omega_\square} \sigma_{c,xx}\, d\Omega + \int_{\Gamma_{r,\square}} N_r e_{1,x}^2\, d\Gamma \right], \tag{35}$$

$$\bar{M} = -\frac{1}{|L_\square|}\left[\int_{\Omega_\square} z\sigma_{c,xx}\, d\Omega + \int_{\Gamma_{r,\square}} N_r z e_{1,x}^2\, d\Gamma \right]. \tag{36}$$

Remark 5. For pure beam action in the 1-direction, the transverse faces of the RVE are assumed stress-free (in an effective sense), which is enforced by setting $\bar{M}_{22} = \bar{N}_{22} = \bar{M}_{12} = \bar{N}_{12} = 0$. In contrast, to represent a one-way plate, the Poisson effect must be suppressed. This is achieved through a plane-strain type assumption, imposing $\bar{\kappa}_{22} = \bar{\varepsilon}_{22} = \bar{\kappa}_{12} = \bar{\varepsilon}_{12} = 0$. For the analysis of one-way plates, it is convenient to work in units per unit width, where the averaging is carried out with respect to the mid-plane area $|A_\square|$ of the RVE, see [9].

3. Model calibration and validation

The proposed sectional model is assessed in two steps. First, the model parameters are calibrated using synthetic training data generated from RVE simulations of TRC beams, slabs or shells. Subsequently, the model is validated against an independent dataset comprising strain paths not included in the calibration. The loading histories are defined as generalized strain paths over the domain.

Table 1
Calibrated model parameters for the three studied section heights.

Parameter	$h = 10\,\text{mm}$ ($\rho = 7.3\%$)	$h = 15\,\text{mm}$ ($\rho = 4.9\%$)	$h = 20\,\text{mm}$ ($\rho = 3.7\%$)
Stiffness parameter, C [GPa]	40.3	40.3	40.3
Effective section height, $\tilde{h}$ [mm]	10.0	14.6	19.6
Threshold in tension, k^t [mJ m^{-1}]	13.3	11.0	11.3
Threshold in compression, k^c [mJ m^{-1}]	36.1	43.0	83.9
Tensile softening parameter, β_t [J m^{-1}]	6.09	8.09	11.90
Compressive softening parameter, β_c [J m^{-1}]	252	610	930
Maximum damage, $D_{\max}$ [–]	0.745	0.731	0.761

$$\{(\bar{\varepsilon}, \bar{\kappa}) \mid |\bar{\varepsilon}| \le 0.4 \times 10^{-3},\ |\bar{\kappa}| \le 250\,\text{mm}^{-1}\},$$

with the additional constraint that the response remains within the sectional strength domain. This condition is enforced by terminating each simulation once the compressive stress in the concrete reaches its strength or the maximum tensile stress in the yarns exceeds the strength.

Four classes of generalized strain paths are considered:

 (i) cyclic axial strain at fixed curvature,
 (ii) cyclic curvature at fixed axial strain,
 (iii) proportional (radial) loading, and
 (iv) sequential loading along the strain axes.

Calibration and validation are performed for three different sections with heights of $h = 10\,\text{mm}$, $h = 15\,\text{mm}$, and $h = 20\,\text{mm}$. Since the reinforcement amount is kept constant across these sections, the reinforcement ratio decreases with increasing section height. The corresponding calibration and validation results are presented in the following subsections.

3.1. Model calibration

The training set contains 16 generalized strain histories, see Appendix F. Due to the symmetry of the cross section, the strain energy release rate at damage onset is identical for the upper and lower parts, i.e., $k_u^t = k_l^t$ and $k_u^c = k_l^c$, so it suffices to calibrate k^t and k^c. Likewise, the damage evolution parameters are symmetric, i.e., $\beta_u^t = \beta_l^t$ and $\beta_u^c = \beta_l^c$, reducing the calibration to β^t and β^c. In addition, the effective stiffness parameter C and effective thickness $\tilde{h}$ are calibrated. The width of the effective section is taken equal to that of the reference RVE, i.e., $\tilde{b} = b$, and is therefore not included among the calibration parameters. The model parameters are estimated in MATLAB using the *fmincon* optimization routine. The objective function is formulated as a convex combination of the average relative error for the set, defined as

$$E(\hat{X}, X) = \frac{1}{G} \sum_{g=1}^{G} \frac{\|\hat{X}^{(g)}(\theta) - X^{(g)}\|_2}{\|X^{(g)}\|_2}, \tag{37}$$

where $\hat{X}^{(g)}$ denotes the predicted values for path g and $X^{(g)}$ the corresponding reference values. The overall objective function is then obtained as

$$J(\theta) = \frac{c_N}{c_N + c_M} E(\hat{N}, N) + \frac{c_M}{c_N + c_M} E(\hat{M}, M). \tag{38}$$

In this case, $c_M = c_N = 1$, meaning that the membrane force and bending moment are equally weighted.

The effective model is implemented in MATLAB, and the calibrated parameters are summarized in Table 1. From these calibrated values, two notable observations can be made. First, the stiffness parameter coincides with the Young's modulus of the concrete ($E = 40.3$ GPa, cf. Appendix E), which is expected since this parameter governs the initial slope of the response in both the resolved and effective models. Second, the effective height closely matches that of the reference section. Finally,

the threshold strain energy release rate remains approximately constant in tension, reflecting the size effect observed for cracking specimens, as described by Bažant [30].

Remark 6. For pure bending the energy release rates in tension scale as $k^t \propto h(\varepsilon_0^t)^2$, so constant k^t implies

$$\varepsilon_0^t \propto h^{-1/2}. \tag{39}$$

This matches Bažant's classical size-effect law [30],

$$\varepsilon_0^t(h) = \frac{f_t'}{E} \frac{1}{\sqrt{1 + h/h_a}}, \tag{40}$$

in which f_t' is the material (or nominal) tensile strength measured on small specimens. This expression reduces to the same $h^{-1/2}$ dependency in the case of scale separation ($h \gg h_a$). This means that the constant threshold for the strain-energy release rate in tension is not coincidental, but a direct manifestation of the size effect. See Appendix D for further details.

Unlike tension, compression damage is less localized and therefore does not exhibit the same size effect. The higher calibrated thresholds k^c for larger sections can instead be attributed to the increase in strain energy release rate with section height. Finally, the maximum damage parameter is also found to be roughly constant across all cases.

3.2. Model validation

The validation set comprises eight strain paths from the same domain as the training data but shifted, translated, and scaled, as illustrated in Fig. 7. The strain paths are illustrated in Fig. 7.

The results for three representative validation paths are shown in Figs. 9–11, corresponding to a cyclic axial path, a cyclic curvature path, and a sequential path, respectively. Results for the remaining loading paths are provided in Appendix H. As shown in Fig. 9, the model reproduces both the moment and normal-force responses with good accuracy across all section heights, showing particularly strong agreement for the moment in the thinnest section. Similarly, Fig. 10 demonstrates that the
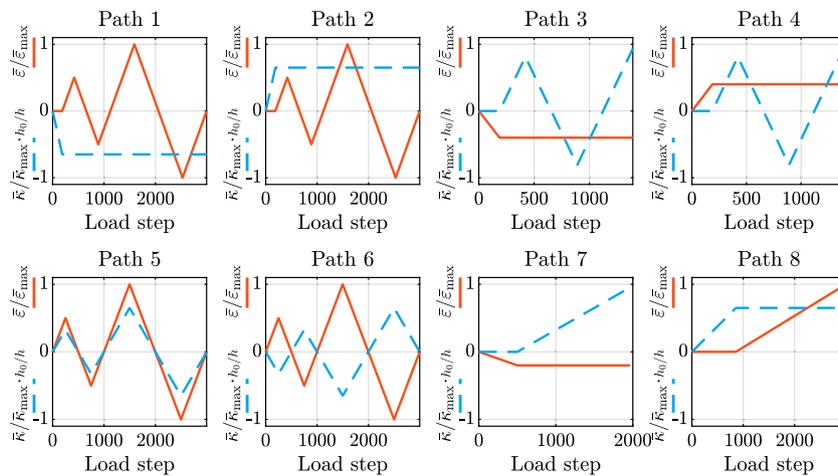
Fig. 7. Generalized strain paths used for validation of the model. $\bar{\varepsilon}$ are normalized by $\bar{\varepsilon}_{\max} = 0.40 \cdot 10^{-3}$ (maximum across all paths), and $\bar{\kappa}$ by $\bar{\kappa}_{\max} = 0.37\,\text{m}^{-1}$ (maximum at $h = 10$ mm), with the section height further normalized by the reference $h = 10$ mm.
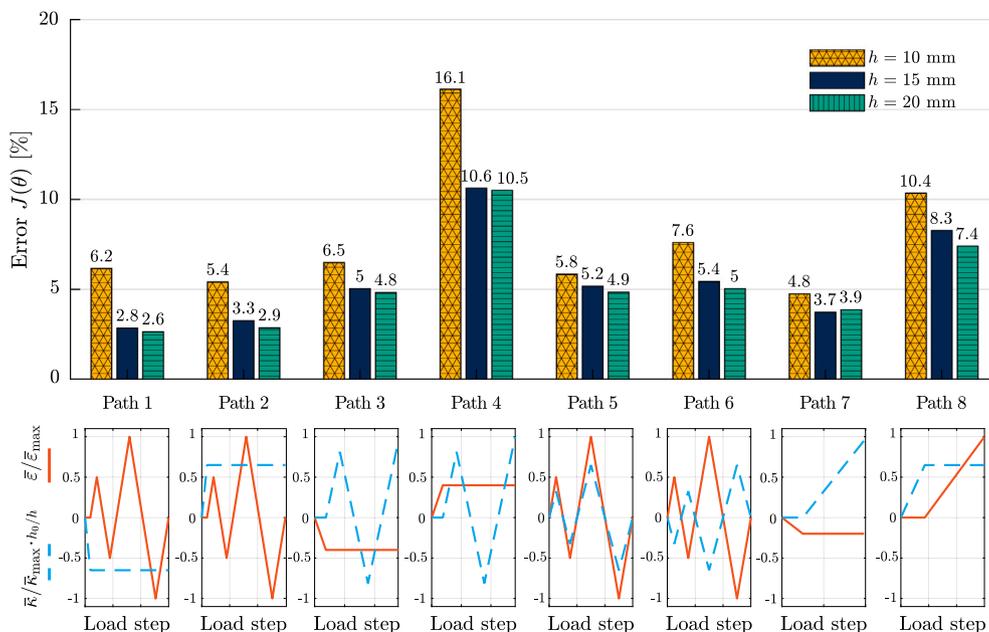
Fig. 8. Error $J(\theta)$ (%) for each load path in Fig. 7 across the three section heights.
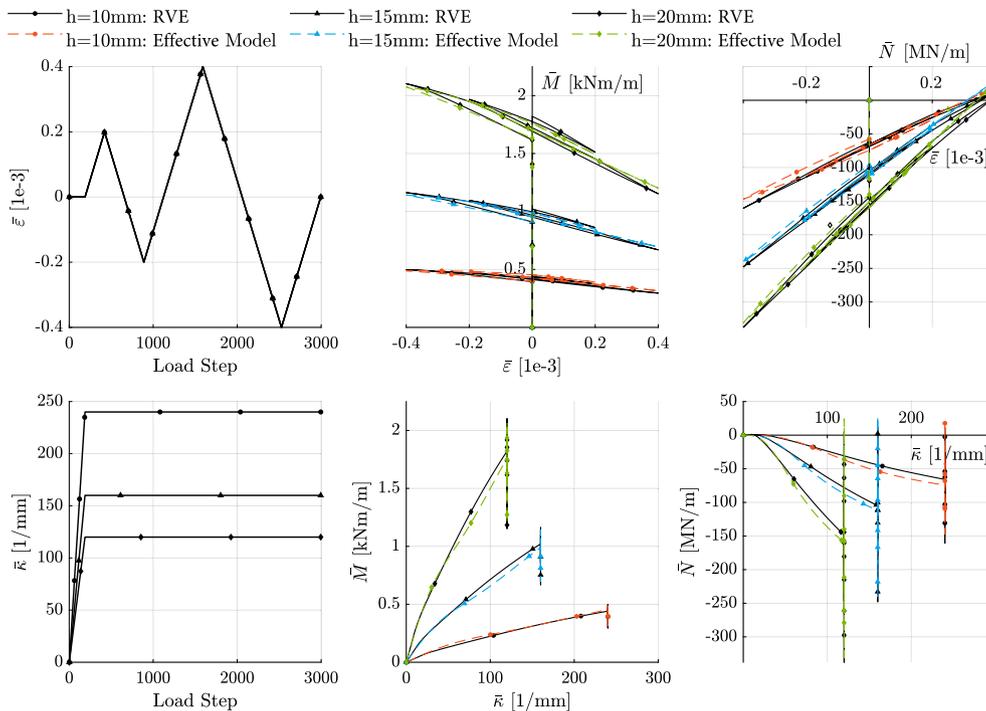
Fig. 9. Comparison of generalized quantities from effective and RVE model for strain path 2.
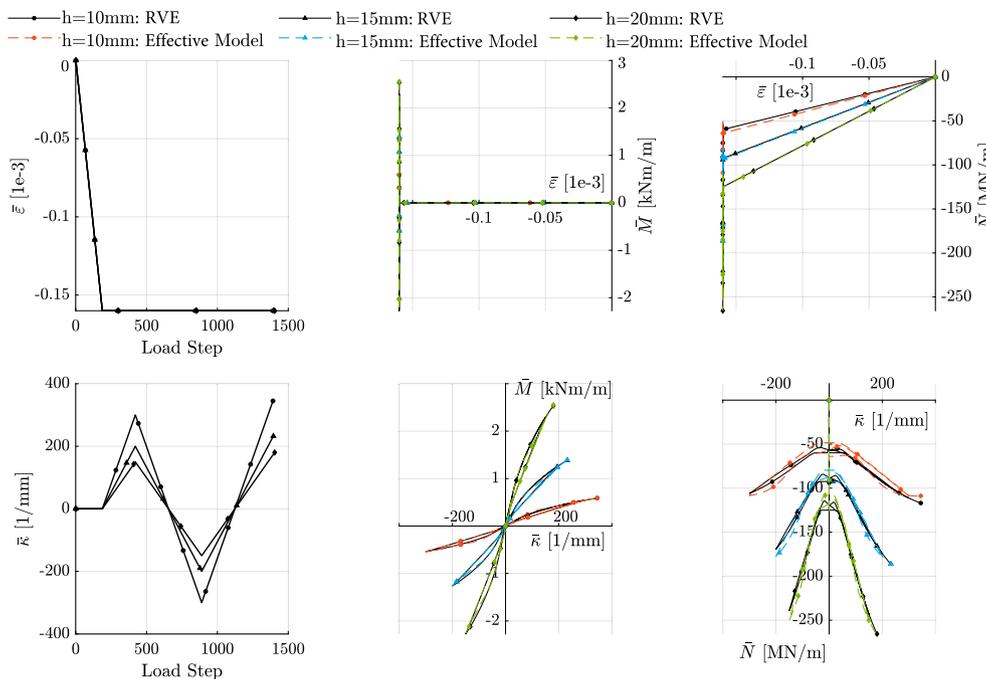

Fig. 10. Comparison of generalized quantities from effective and RVE model for strain path 3.

moment–curvature relation is captured with high accuracy for all section heights, whereas the normal-force response exhibits slightly improved agreement for thicker sections. At small curvature values, however, the model does not fully reproduce the rapid fluctuations in normal force observed in the reference results. For the sequential loading case in Fig. 11, the model slightly overestimates the normal force in the thinner sections but generally captures the increase in compressive normal force associated with crack initiation.

The relative errors, computed according to Eq. (38), are summarized for all validation paths in Fig. 8. Two loading paths stand out: path 4 (cyclic bending under constant axial tension) and path 8 (sequential loading with initial positive bending followed by axial tension). These results indicate that the model captures loading scenarios involving axial compression more accurately than those dominated by axial tension. The overall error, averaged over all loading paths, decreases with increasing section height. The effect is most pronounced for $h = 10$ mm,
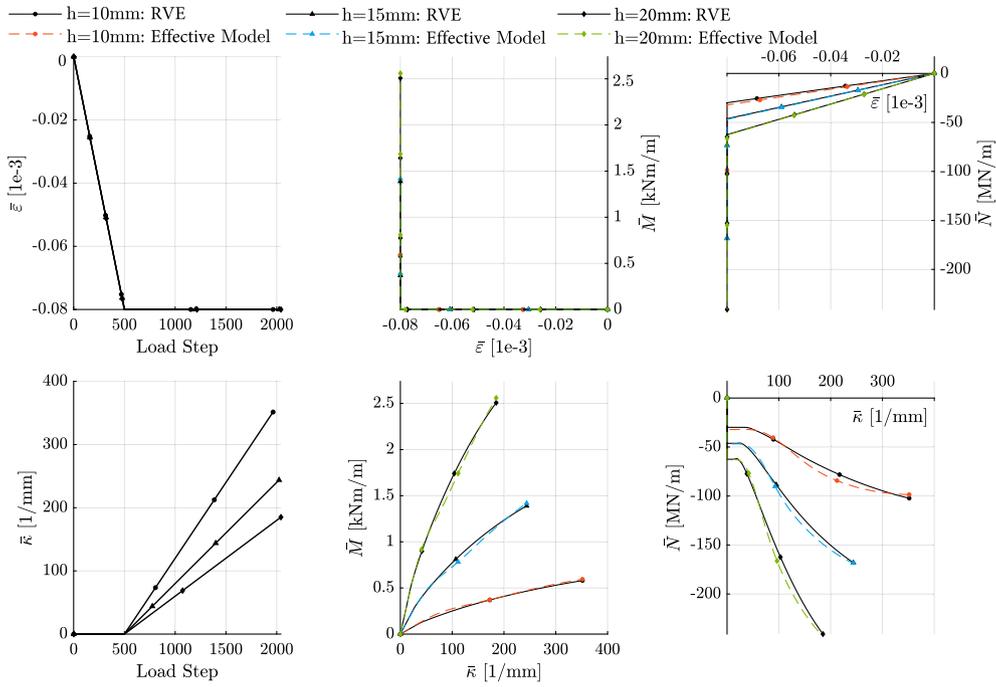
Fig. 11. Comparison of generalized quantities from effective and RVE model for strain path 7.
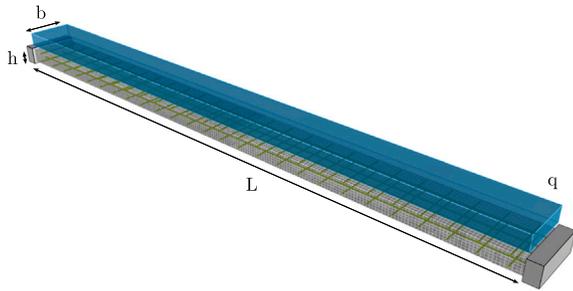

Fig. 12. Geometry, boundary conditions and load for the TRC slab used in the case study.

where $J(\theta) = 7.8\ \%$, and reduces to $J(\theta) = 5.6\ \%$ and $J(\theta) = 5.3\ \%$ for $h = 15$ mm and $h = 20$ mm, respectively. This trend may be partly explained by the decreasing reinforcement ratio with increasing height, which reduces the relative influence of the reinforcement and leads to a more homogeneous sectional response.

3.3. Case study: comparison with fully resolved one-way TRC slab

To evaluate the performance of the effective model, its predictions are compared against those obtained from a fully resolved direct numerical simulation (DNS) of a one-way slab with fixed ends subjected to a uniform surface-load q. The studied slab is 650 mm long, has a height of 15 mm and a width of 50 mm, see Fig. 12. The fully resolved model uses the same material parameters as the RVE, see Appendix E. The effective
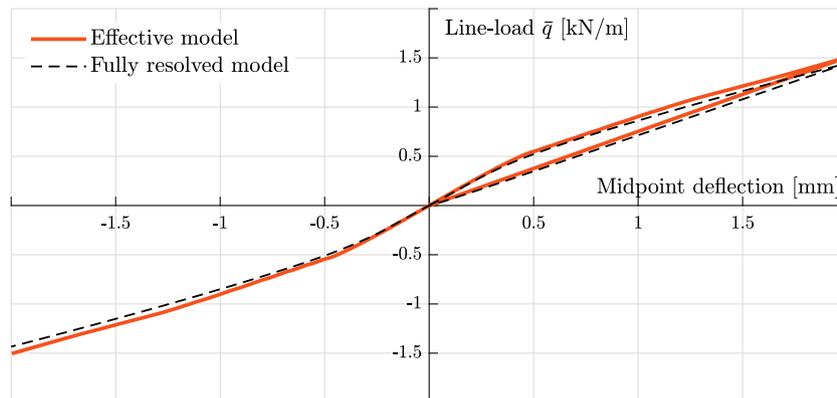

Fig. 13. Comparison between the load versus mid-point deflection curves obtained using a fully resolved simulation and the effective model. For the fully resolved model the line-load $\bar{q}$ is obtained by multiplying the surface load q by the width of the slab.
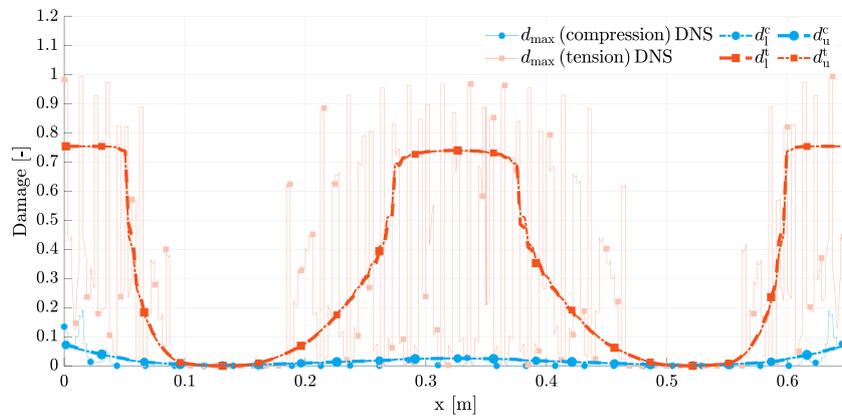
Fig. 14. The variation of the maximum attained values of damage variables along the slab for the effective model. Also plotted is the maximum attained tensile and compressive damage (averaged over the width) for the outermost fibers of the fully resolved model.
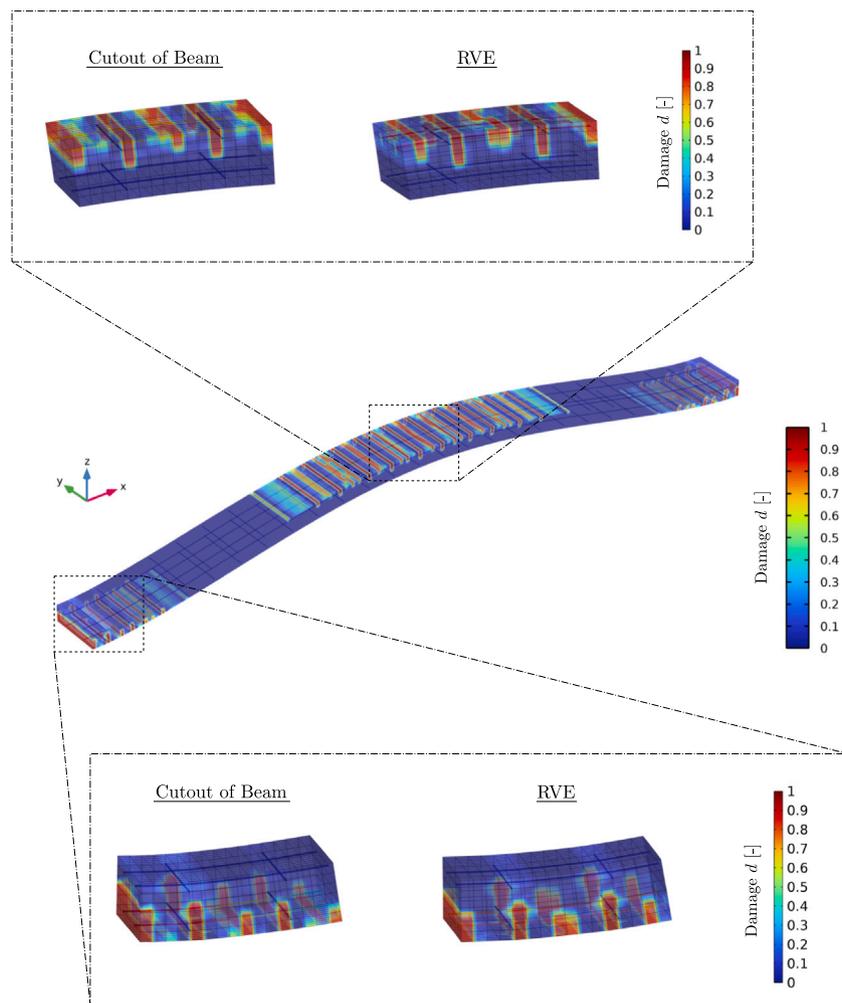

Fig. 15. Comparison of local damage fields for a one-way textile-reinforced concrete slab. The figure in the middle shows the damage field from a fully resolved three-dimensional finite element simulation. At two selected Gauss points, generalized strain histories are extracted from the effective beam model and applied as prescribed loading to representative volume element simulations, whose resulting damage fields are shown for comparison.

model is implemented as an FE beam model in MATLAB, and is solved incrementally using an adaptive step size and the Newton–Raphson method under displacement control of the mid-point node using the tangent stiffness in Eq. (23). The slab model is discretized into 100 beam elements with cubic Hermite shape functions for $\bar{w}$ and linear shape functions for $\bar{u}$.

The comparison between the fully resolved model and the effective slab model in terms of the load magnitude and the midpoint deflection is shown in Fig. 13. Generally, the effective model is able to predict the strain-hardening response under cyclic loading. The fully resolved simulation requires approximately 40 h, whereas the effective slab model can be solved in only 0.2 h, representing a speed-up of nearly two orders
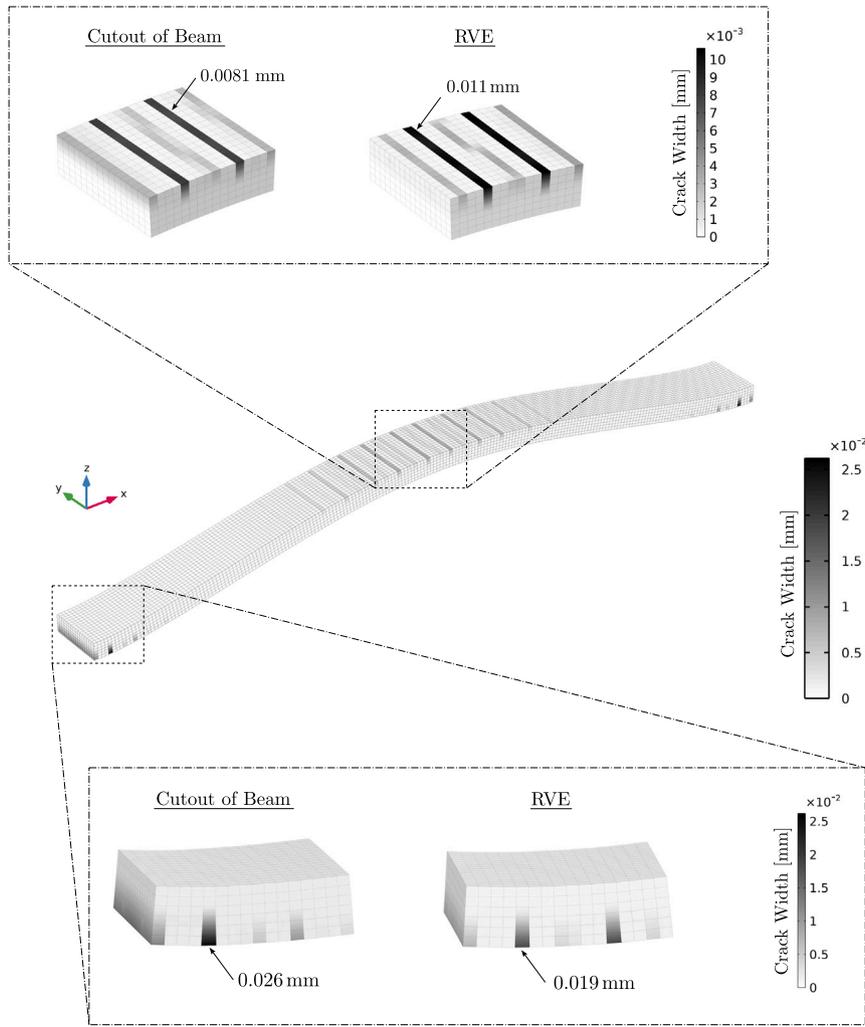
Fig. 16. Computed crack widths for the fully resolved model at the state of maximum positive deflection and a comparison with the result obtained when subjecting the RVE to the strain history from the effective model.

of magnitude for the considered problem and implementation.[2] The relative error for a specific midpoint deflection δ_{mid}, defined as

$$e_{\text{rel}}(\delta_{\text{mid}}) = \frac{\left| \bar{q}_{\text{eff}}(\delta_{\text{mid}}) - \bar{q}_{\text{ref}}(\delta_{\text{mid}}) \right|}{\bar{q}_{\text{ref}}(\delta_{\text{mid}})}, \tag{41}$$

over the entire load–deflection history, reaches a maximum of 4.9 %. Additionally, inspection of the final damage distribution along the effective slab in Fig. 14 shows that the tensile damage is concentrated at the mid-span and near the supports, while the compressive damage is more widely distributed. In these regions, the effective damage reaches values close to D_{max} reported in Table 1. A comparison between the effective model and the fully resolved model indicates that the effective damage, in some sense, represents an averaging of the localized damage predicted by the fully resolved model. It should be noted, however, that

the effective model does not exhibit damage localization, which is consistent with the large-scale strain-hardening response typically observed in TRC [31].

A more detailed comparison is obtained by examining the local response. Since the effective structural model does not explicitly resolve local damage fields, the generalized strain histories are extracted at two selected Gauss points in the beam model and subsequently applied as prescribed loading to RVE simulations, see Fig. 1. The resulting damage fields are then compared to those obtained from the fully resolved three-dimensional slab simulation. This comparison, shown in Fig. 15, illustrates that the effective model reproduces the macroscopic strain evolution, while the representative volume element driven by this strain history captures the corresponding damage mechanisms with good qualitative agreement. Local discrepancies near the representative volume element boundaries are expected due to the use of periodic boundary conditions.

A similar comparison can also be made in terms of crack widths. The crack widths are obtained by integrating the strain component normal to the cracks over a distance corresponding to the crack-band width h_{cb} (equal to the element size in this case), see Fig. 16. The figure shows that the crack pattern, and consequently the crack spacing, is well captured, and that the crack width is predicted with reasonable accuracy. At the midpoint of the slab, the maximum crack width predicted by the RVE is 0.011 mm, compared to 0.0081 mm from the fully resolved analysis. At

---

[2] The effective beam model was solved on a 10-core Intel® Core™ i7 laptop (32 GB RAM), requiring approximately 0.2 h of wall-clock time. The fully resolved model was solved on an AMD EPYC 9354 cluster node (773 GB RAM) with 16 cores assigned, with a total runtime of 40 h. This corresponds to an apparent $200\times$ wall-clock speedup and at least a $320\times$ reduction in core-hours, although actual core utilization was not monitored.

the support, the difference is larger, with the RVE predicting 0.019 mm compared to 0.026 mm in the fully resolved case. Notably, the effective model combined with the RVE slightly overestimates the crack width at the midpoint, while underestimating it near the support. This can be attributed to the fact that the RVE provides an averaged local response and does not explicitly represent the fixed boundary condition at the support.

4. Conclusions and outlook

In this work, we propose an efficient constitutive model for uniaxial members such as beams. The key novelty of the proposed formulation lies in its ability to predict the *fully coupled response between normal force and bending moment under cyclic and non-proportional loading conditions*, while accounting for tensile and compressive damage at the sectional level. The model is formulated at the global cross-sectional level, thus eliminating the need for explicit evaluation of the local material response across the section. Stiffness degradation is governed by global damage variables associated with the upper and lower regions of the section, whose evolution depends on the sign of the strain, thereby capturing crack opening and closure effects and enabling a fully coupled normal force–bending moment response under general loading histories. The model is applicable to uniaxial members subjected to combined axial load and bending. In particular, the model is well-suited for the analysis of one-way TRC slabs and shells, as it accurately reproduces the strain-hardening response characteristic of these structures.

The formulation was calibrated using data obtained from representative volume element (RVE) simulations of the TRC substructure. These simulations provide essential information about the subscale interactions between the yarns and the surrounding concrete. The model was first validated against synthetic RVE data at the cross-sectional level. It was able to predict the evolution of both the normal force and the bending moment with an overall relative error of around 5–8 %. Despite its reduced-order nature, the effective formulation reproduces the coupled sectional response with good accuracy while achieving a reduction in computational cost of approximately two orders of magnitude, as demonstrated in a one-way TRC slab case study. The reported speed-up should be interpreted as reflecting the reduction in computational complexity achieved by replacing RVE-based multiscale simulations with the proposed reduced-order sectional formulation; absolute runtimes will depend on the specific problem, discretization, and implementation.

The proposed framework can be applied to investigate the cyclic response of one-way TRC members. It is particularly suited for general loading histories in which normal force and bending moment evolve in a coupled manner due to damage. It captures the strain-hardening effects associated with cracking and crushing, enabling for instance prediction of stress redistribution within the structure. Since cracking is represented only implicitly, however, the effective model does not directly provide crack spacing or crack width. These local quantities can instead be recovered in a post-processing step by applying the generalized strain histories obtained from the effective model to the RVE, as demonstrated in Section 3.3.

The approach is particularly suited for beams and one-way plates where the nonlinear response is governed mainly by damage mechanisms. When the subscale behavior involves additional mechanisms, such as residual bond slip [32], plastic strains in compressed concrete [33,34], plastic deformation of the reinforcement, or incomplete crack closure [35], the effective response includes permanent deformations. Capturing such effects would require extending the present damage-based framework toward a combined damage–plasticity formulation, as proposed in [36,37], and constitutes a natural direction for future work.

In its present form, the model does not consider localization, meaning that direct application to problems with large-scale localization would lead to mesh-dependent results; hence, appropriate regularization is required before it can be used in such scenarios. Moreover, the current formulation is restricted to one-way action. Extending the proposed surrogate concept to two-dimensional plate or shell formulations therefore constitutes a natural and promising direction for future work, with the potential to further bridge the gap between detailed multiscale modeling and efficient structural-scale analysis.

CRediT authorship contribution statement

Gabriel Edefors: Writing – original draft, Visualization, Validation, Methodology, Investigation, Formal analysis, Conceptualization. **Fredrik Larsson:** Writing – review & editing, Supervision, Methodology, Investigation, Formal analysis, Conceptualization. **Karin Lundgren:** Writing – review & editing, Supervision, Methodology, Investigation, Formal analysis, Conceptualization.

Declaration of generative AI and AI-assisted technologies in the writing process

During the preparation of this work the authors used ChatGPT to improve spelling and grammar. After using this tool, the authors reviewed and edited the content as needed and take full responsibility for the content of the publication.

Declaration of competing interest

The authors declare that they have no known competing financial interests or personal relationships that could have appeared to influence the work reported in this paper.

Acknowledgements

Appendix A. Degraded generalized stresses

The generalized stresses, i.e., the thermodynamic forces conjugate to the generalized strains, are obtained as the partial derivatives of the generalized Helmholtz free energy density with respect to the generalized strains.

Normal force. The normal force is evaluated as

$$\bar{N} = \frac{\partial \bar{\Psi}}{\partial \bar{\varepsilon}}\bigg|_{\bar{\kappa},\bar{d}}. \tag{A.1}$$

To evaluate this derivative, consider a finite variation $\Delta\bar{\varepsilon}$. The corresponding variation of the generalized free energy reads

$$\Delta\bar{\Psi} = \bar{\Psi}(\bar{\varepsilon} + \Delta\bar{\varepsilon}, \bar{\kappa}, \bar{d}) - \bar{\Psi}(\bar{\varepsilon}, \bar{\kappa}, \bar{d}), \tag{A.2}$$

and the derivative is obtained from the limit

$$\bar{N} = \lim_{\Delta\bar{\varepsilon}\to 0} \frac{\Delta\bar{\Psi}}{\Delta\bar{\varepsilon}}. \tag{A.3}$$
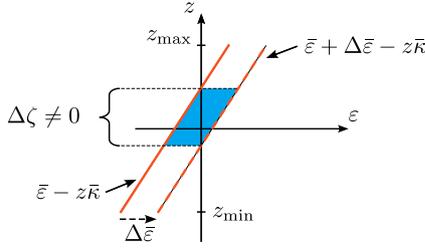
Using Eq. (13), we may express

$$\Delta\bar{\Psi} = \int_A \left[\zeta(\bar{\varepsilon}, \bar{\kappa}, \bar{d})\,\Delta\Psi^0 + C^{\varepsilon}(\Delta\bar{\varepsilon}) \right] \mathrm{d}A, \tag{A.4}$$

where

$$C^{\varepsilon}(\Delta\bar{\varepsilon}) = \Delta\zeta\,\Psi^0(\bar{\varepsilon} + \Delta\bar{\varepsilon} - z\bar{\kappa}), \tag{A.5}$$

and

$$\Delta\Psi^0 = \Psi^0(\bar{\varepsilon} + \Delta\bar{\varepsilon} - z\bar{\kappa}) - \Psi^0(\bar{\varepsilon} - z\bar{\kappa}), \tag{A.6}$$

Fig. A.17. Variation $\Delta\bar{\varepsilon}$ applied to the strain profile in the section and the region where the jump in the damage activation function $\Delta\zeta$ is nonzero.

$$\Delta\zeta = \zeta(\bar{\varepsilon} + \Delta\bar{\varepsilon}, \bar{\kappa}, \bar{d}) - \zeta(\bar{\varepsilon}, \bar{\kappa}, \bar{d}). \tag{A.7}$$

We first note that the jump $\Delta\zeta$ is nonzero only where $\text{sign}(\bar{\varepsilon} + \Delta\bar{\varepsilon} - z\bar{\kappa}) \neq \text{sign}(\bar{\varepsilon} - z\bar{\kappa})$, and that its magnitude is bounded according to

$$\left|\Delta\zeta(z)\right| \le \left|d^{\mathrm{c}}(z) - d^{\mathrm{t}}(z)\right| \le 1, \tag{A.8}$$

since $d^{\mathrm{c}}, d^{\mathrm{t}} \in [0, 1]$.

Second, it can be verified algebraically that

$$|\bar{\varepsilon} + \Delta\bar{\varepsilon} - z\bar{\kappa}| \le |\Delta\bar{\varepsilon}|, \tag{A.9}$$

on the domain where $\Delta\zeta \neq 0$, cf. the illustration in Fig. A.17.

Third, using the explicit form of the undamaged local free energy density Ψ^0 from Eq. (4) together with the inequality in Eq. (A.9), we conclude that

$$\Psi^0(\bar{\varepsilon} + \Delta\bar{\varepsilon} - z\bar{\kappa}) \le \tfrac{1}{2} C(z)(\Delta\bar{\varepsilon})^2. \tag{A.10}$$

Combining Eqs. (A.10) and (A.8) allows us to bound $C^\varepsilon(\Delta\bar{\varepsilon})$ as

$$\left|C^\varepsilon(\Delta\bar{\varepsilon})\right| = \left|\Delta\zeta\,\Psi^0(\bar{\varepsilon} + \Delta\bar{\varepsilon} - z\bar{\kappa})\right| \le \tfrac{1}{2}C(z)(\Delta\bar{\varepsilon})^2, \quad \text{for } \Delta\zeta \neq 0. \tag{A.11}$$

Evaluating the limit in Eq. (A.3) gives

$$\bar{N} = \lim_{\Delta\bar{\varepsilon}\to 0} \left[\int_A \zeta(\bar{\varepsilon}, \bar{\kappa}, \bar{d})\frac{\Delta\Psi^0}{\Delta\bar{\varepsilon}}\,\mathrm{d}A + R^\varepsilon(\Delta\bar{\varepsilon})\right], \tag{A.12}$$

where

$$R^\varepsilon(\Delta\bar{\varepsilon}) := \int_A \frac{C^\varepsilon(\Delta\bar{\varepsilon})}{\Delta\bar{\varepsilon}}\,\mathrm{d}A. \tag{A.13}$$

From Eqs. (A.13) and (A.11), it follows that

$$\left|R^\varepsilon(\Delta\bar{\varepsilon})\right| \le A\,C_{\max}\,|\Delta\bar{\varepsilon}|, \tag{A.14}$$
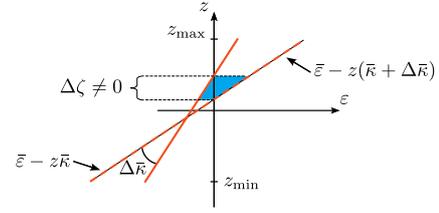
where $C_{\max} := \sup_{z\in A} C(z)$. Hence

$$R^\varepsilon(\Delta\bar{\varepsilon}) \to 0 \quad \text{as} \quad \Delta\bar{\varepsilon} \to 0, \tag{A.15}$$

whereby

$$\bar{N} = \int_A \zeta(\bar{\varepsilon}, \bar{\kappa}, \bar{d})\frac{\partial\Psi^0}{\partial\bar{\varepsilon}}\,\mathrm{d}A = \underbrace{\int_A C(z)\,\zeta(\bar{\varepsilon}, \bar{\kappa}, \bar{d})\,\mathrm{d}A}_{\bar{C}_{\mathrm{A}}}\,\bar{\varepsilon}$$

$$- \underbrace{\int_A C(z)z\,\zeta(\bar{\varepsilon}, \bar{\kappa}, \bar{d})\,\mathrm{d}A}_{\bar{C}_{\mathrm{S}}}\,\bar{\kappa}, \tag{A.16}$$

that is,

$$\bar{N} = \bar{C}_{\mathrm{A}}\bar{\varepsilon} - \bar{C}_{\mathrm{S}}\bar{\kappa}. \tag{A.17}$$

Fig. A.18. Variation $\Delta\bar{\kappa}$ applied to the strain profile in the section and the region where the jump in the damage activation function $\Delta\zeta$ is nonzero.

Bending moment. The bending moment is evaluated as

$$\bar{M} = \frac{\partial\bar{\Psi}}{\partial\bar{\kappa}}\bigg|_{\bar{\varepsilon},\bar{d}}. \tag{A.18}$$

Following the same procedure as for the normal force, consider a finite variation $\Delta\bar{\kappa}$ and write

$$\bar{M} = \lim_{\Delta\bar{\kappa}\to 0}\frac{\Delta\bar{\Psi}}{\Delta\bar{\kappa}}, \qquad \Delta\bar{\Psi} = \int_A \left[\zeta(\bar{\varepsilon}, \bar{\kappa}, \bar{d})\,\Delta\Psi^0 + C^\kappa(\Delta\bar{\kappa})\right]\mathrm{d}A, \tag{A.19}$$

where

$$C^\kappa(\Delta\bar{\kappa}) = \Delta\zeta\,\Psi^0\big(\bar{\varepsilon} - z(\bar{\kappa} + \Delta\bar{\kappa})\big), \qquad \Delta\Psi^0 = \Psi^0\big(\bar{\varepsilon} - z(\bar{\kappa} + \Delta\bar{\kappa})\big) - \Psi^0\big(\bar{\varepsilon} - z\bar{\kappa}\big). \tag{A.20}$$

As in the axial case, the jump $\Delta\zeta$ is nonzero only where

$$\text{sign}(\bar{\varepsilon} - z(\bar{\kappa} + \Delta\bar{\kappa})) \neq \text{sign}(\bar{\varepsilon} - z\bar{\kappa}),$$

and its magnitude satisfies

$$\left|\Delta\zeta(z)\right| \le \left|d^{\mathrm{c}}(z) - d^{\mathrm{t}}(z)\right| \le 1, \tag{A.21}$$

since $d^{\mathrm{c}}, d^{\mathrm{t}} \in (0, 1)$. On the same domain ($\Delta\zeta \neq 0$), the local strains satisfy

$$\left|\bar{\varepsilon} - z(\bar{\kappa} + \Delta\bar{\kappa})\right| \le |z\,\Delta\bar{\kappa}|. \tag{A.22}$$

Using the explicit form of Ψ^0 in Eqs. (4) and (A.22), we obtain

$$\Psi^0\big(\bar{\varepsilon} - z(\bar{\kappa} + \Delta\bar{\kappa})\big) \le \tfrac{1}{2}\,C(z)\,z^2(\Delta\bar{\kappa})^2. \tag{A.23}$$

Combining (A.21) and (A.23) yields the bound

$$\left|C^\kappa(\Delta\bar{\kappa})\right| = \left|\Delta\zeta\,\Psi^0\big(\bar{\varepsilon} - z(\bar{\kappa} + \Delta\bar{\kappa})\big)\right| \le \tfrac{1}{2}\,C(z)\,z^2(\Delta\bar{\kappa})^2, \quad \text{for } \Delta\zeta \neq 0. \tag{A.24}$$

Substituting into the limit definition gives

$$\bar{M} = \lim_{\Delta\bar{\kappa}\to 0}\left[\int_A \zeta(\bar{\varepsilon}, \bar{\kappa}, \bar{d})\frac{\Delta\Psi^0}{\Delta\bar{\kappa}}\,\mathrm{d}A + R^\kappa(\Delta\bar{\kappa})\right], \tag{A.25}$$

where

$$R^\kappa(\Delta\bar{\kappa}) := \int_A \frac{C^\kappa(\Delta\bar{\kappa})}{\Delta\bar{\kappa}}\,\mathrm{d}A. \tag{A.26}$$

From (A.24), introducing the beam height $|z| \le \tilde{h}/2$, and $C(z) \le C_{\max} := \sup_{z\in A} C(z)$, we obtain

$$\left|R^\kappa(\Delta\bar{\kappa})\right| \le \tfrac{1}{4}\,A\,C_{\max}\,\tilde{h}^2\,|\Delta\bar{\kappa}|, \tag{A.27}$$

Hence

$$R^\varepsilon(\Delta\bar{\varepsilon}) \to 0 \quad \text{as} \quad \Delta\bar{\varepsilon} \to 0, \tag{A.28}$$

whereby

$$\bar{M} = \int_A \zeta(\bar{\varepsilon}, \bar{\kappa}, \bar{d})\frac{\partial\Psi^0}{\partial\bar{\kappa}}\,\mathrm{d}A = \underbrace{\int_A z^2\,C(z)\,\zeta(\bar{\varepsilon}, \bar{\kappa}, \bar{d})\,\mathrm{d}A}_{\bar{C}_{\mathrm{I}}}\,\bar{\kappa}$$

$$-\underbrace{\int_A z\, C(z)\, \zeta(\bar\varepsilon, \bar\kappa, \bar{\boldsymbol{d}})\, \mathrm{d}A}_{\bar{C}_{\mathrm{S}}}\ \bar\varepsilon, \tag{A.29}$$

that is,

$$\bar M = \bar{C}_{\mathrm{I}}\bar\kappa - \bar{C}_{\mathrm{S}}\bar\varepsilon. \tag{A.30}$$

Appendix B. Degraded generalized stress tangents

The tangent stiffness matrix is defined as the matrix of second derivatives of the generalized free energy, i.e.,

$$\boldsymbol{H} = \begin{bmatrix} \dfrac{\partial^2 \bar\Psi}{\partial \bar\varepsilon^2} & \dfrac{\partial^2 \bar\Psi}{\partial \bar\varepsilon\, \partial \bar\kappa} \\ \dfrac{\partial^2 \bar\Psi}{\partial \bar\kappa\, \partial \bar\varepsilon} & \dfrac{\partial^2 \bar\Psi}{\partial \bar\kappa^2} \end{bmatrix} = \begin{bmatrix} \dfrac{\partial \bar N}{\partial \bar\varepsilon} & \dfrac{\partial \bar N}{\partial \bar\kappa} \\ \dfrac{\partial \bar M}{\partial \bar\varepsilon} & \dfrac{\partial \bar M}{\partial \bar\kappa} \end{bmatrix}. \tag{B.1}$$

The components of $\boldsymbol{H}$ are evaluated in direct analogy with the degraded generalized stresses $\bar N$ and $\bar M$ derived in Appendix A. For illustrative purposes, the detailed derivation of $\partial \bar N / \partial \bar\varepsilon$ is presented below.

To evaluate this derivative, we introduce a finite variation $\Delta\bar\varepsilon \in \mathbb{R}$. The corresponding variation in the normal force is given by

$$\Delta \bar N = \int_A \left[\zeta(\bar\varepsilon + \Delta\bar\varepsilon, \bar\kappa, \bar{\boldsymbol{d}})\, C(z)\,(\bar\varepsilon + \Delta\bar\varepsilon - z\bar\kappa) - \zeta(\bar\varepsilon, \bar\kappa, \bar{\boldsymbol{d}})\, C(z)\,(\bar\varepsilon - z\bar\kappa) \right] \mathrm{d}A \tag{B.2}$$

$$= \int_A \left[\zeta(\bar\varepsilon, \bar\kappa, \bar{\boldsymbol{d}})\, C(z)\, \Delta\bar\varepsilon + C^{\varepsilon\varepsilon}(\Delta\bar\varepsilon) \right] \mathrm{d}A, \tag{B.3}$$

where we have introduced

$$C^{\varepsilon\varepsilon}(\Delta\bar\varepsilon) := \Delta\zeta\, C(z)\,(\bar\varepsilon + \Delta\bar\varepsilon - z\bar\kappa). \tag{B.4}$$

The derivative of $\bar N$ with respect to $\bar\varepsilon$ then follows from the limit

$$\frac{\partial \bar N}{\partial \bar\varepsilon} = \lim_{\Delta\bar\varepsilon \to 0} \frac{\Delta \bar N}{\Delta\bar\varepsilon}. \tag{B.5}$$

We distinguish the following two mutually exclusive and exhaustive cases:

$$\begin{cases} (i) & \bar\varepsilon \neq 0,\ \bar\kappa = 0, \\ (ii) & \bar\kappa \neq 0,\ \bar\varepsilon \in \mathbb{R}. \end{cases}$$

Case (i). For $\bar\varepsilon \neq 0$ and $\bar\kappa = 0$, the jump $\Delta\zeta = 0$ for any $|\Delta\bar\varepsilon| \leq |\bar\varepsilon|$. Consequently, in the limit $\Delta\bar\varepsilon \to 0$, $\Delta\zeta \to 0$, and the derivative in (B.5) simplifies to

$$\frac{\partial \bar N}{\partial \bar\varepsilon} = \lim_{\Delta\bar\varepsilon \to 0} \int_A \zeta(\bar\varepsilon, \bar\kappa, \bar{\boldsymbol{d}})\, C(z)\, \mathrm{d}A = \bar{C}_{\mathrm{A}}. \tag{B.6}$$

Case (ii). From Eq. (B.6) it follows that it suffices to show that the residual vanishes, i.e.,

$$R^{\varepsilon\varepsilon} = \int_A \frac{C^{\varepsilon\varepsilon}(\Delta\bar\varepsilon)}{\Delta\bar\varepsilon}\, \mathrm{d}A \longrightarrow 0 \quad \text{as} \quad \Delta\bar\varepsilon \to 0, \tag{B.7}$$

for the case $\bar\kappa \neq 0$ and $\bar\varepsilon \in \mathbb{R}$. To this end, we perform the integration only over the subset of the cross section where $\Delta\zeta \neq 0$. We denote this active region by

$$\int_{A\,:\,\Delta\zeta \neq 0} \mathrm{d}A = \tilde b\, \Delta\tilde h,$$

where we recall $\tilde b$ as the width of the section and $\Delta\tilde h$ as the height of the region in which $\Delta\zeta \neq 0$ for a given increment $\Delta\bar\varepsilon$. Accordingly, the

integral can be expressed as

$$R^{\varepsilon\varepsilon} = \int_A C^{\varepsilon\varepsilon}(\Delta\bar\varepsilon)\, \mathrm{d}A = \int_{A\,:\,\Delta\zeta \neq 0} C^{\varepsilon\varepsilon}(\Delta\bar\varepsilon)\, \mathrm{d}A. \tag{B.8}$$

We shall now bound this region using the strain increment. To this end, we identify the following identities[3]:

$$\begin{cases} \bar\varepsilon + \Delta\bar\varepsilon - z\bar\kappa > 0 \ \Leftrightarrow\ z < \dfrac{\bar\varepsilon + \Delta\bar\varepsilon}{\bar\kappa}, \\ \bar\varepsilon - z\bar\kappa < 0 \ \Leftrightarrow\ z > \dfrac{\bar\varepsilon}{\bar\kappa}, \end{cases} \quad \text{for } \Delta\zeta \neq 0,$$

so that the height of the subregion can be written as

$$\Delta\tilde h = |z_{\max} - z_{\min}| = \frac{|\Delta\bar\varepsilon|}{|\bar\kappa|}. \tag{B.9}$$

This makes it possible to bound the subregion according to

$$\tilde b\, \Delta\tilde h \leq \tilde b\, \frac{|\Delta\bar\varepsilon|}{|\bar\kappa|}. \tag{B.10}$$

Finally, using Eqs. (B.10), (A.21), and (A.9), it is possible to bound Eq. (B.8) as

$$|R^{\varepsilon\varepsilon}| = \left| \int_{A\,:\,\Delta\zeta \neq 0} \frac{\Delta\zeta\, C(z)\,(\bar\varepsilon + \Delta\bar\varepsilon - z\bar\kappa)}{\Delta\bar\varepsilon}\, \mathrm{d}A \right|$$

$$\leq \frac{C_{\max}\tilde b}{|\bar\kappa|}\, |\Delta\bar\varepsilon| \longrightarrow 0 \quad \text{as} \quad \Delta\bar\varepsilon \to 0. \tag{B.11}$$

It therefore follows from Eq. (B.6) that

$$\frac{\partial \bar N}{\partial \bar\varepsilon} = \bar{C}_{\mathrm{A}}. \tag{B.12}$$

Appendix C. Degraded strain energy release rates

The strain energy release rates, i.e., the thermodynamic forces conjugate to the damage variables, are obtained as the partial derivatives of the Helmholtz free energy with respect to the components of the damage vector $\bar{\boldsymbol{d}}$, while holding the generalized strains fixed:

$$Y_{\mathrm{u}}^{\mathrm{t/c}} = -\left.\frac{\partial \bar\Psi}{\partial d_{\mathrm{u}}^{\mathrm{t/c}}}\right|_{\bar\varepsilon, \bar\kappa} = -\int_{A_{\mathrm{u}}} \frac{\partial \zeta}{\partial d_{\mathrm{u}}^{\mathrm{t/c}}}\, \Psi^0(\varepsilon(z))\, \mathrm{d}A - \int_{A_{\mathrm{u}}} \zeta\, \overset{\,0}{\cancel{\frac{\partial \Psi^0}{\partial d_{\mathrm{u}}^{\mathrm{t/c}}}}}\, \mathrm{d}A$$

$$= \frac{1}{2} \int_{A_{\mathrm{u}}} C(z)\, \langle \bar\varepsilon - z\bar\kappa \rangle_{\mathrm{t/c}}^2\, \mathrm{d}A, \tag{C.1a}$$

$$Y_{\mathrm{l}}^{\mathrm{t/c}} = -\left.\frac{\partial \bar\Psi}{\partial d_{\mathrm{l}}^{\mathrm{t/c}}}\right|_{\bar\varepsilon, \bar\kappa} = -\int_{A_{\mathrm{l}}} \frac{\partial \zeta}{\partial d_{\mathrm{l}}^{\mathrm{t/c}}}\, \Psi^0(\varepsilon(z))\, \mathrm{d}A - \int_{A_{\mathrm{l}}} \zeta\, \overset{\,0}{\cancel{\frac{\partial \Psi^0}{\partial d_{\mathrm{l}}^{\mathrm{t/c}}}}}\, \mathrm{d}A$$

$$= \frac{1}{2} \int_{A_{\mathrm{l}}} C(z)\, \langle \bar\varepsilon - z\bar\kappa \rangle_{\mathrm{t/c}}^2\, \mathrm{d}A. \tag{C.1b}$$

Appendix D. Size effect interpretation

This section demonstrates that the size-effect law proposed by Bažant [30] implies a constant threshold for the strain energy release rate. To this end, the case of uniaxial pure bending is considered. From

---

[3] Here we choose $\Delta\bar\varepsilon > 0$. Adopting $\Delta\bar\varepsilon < 0$ would result in the same bound for $\Delta\tilde h$.

Eq. (17a), under pure bending ($\bar{\varepsilon} = 0$), the strain energy release rate is

$$Y_u^t = \frac{1}{2} \int_{A_u} C(z) \left\langle - z\bar{\kappa} \right\rangle_+^2 \, dA = \frac{\bar{\kappa}^2}{2} \int_{A_u} C(z) \, z^2 \, dA = \frac{\bar{\kappa}^2}{2} \bar{C}_I^0 \qquad (D.1)$$

At the onset of damage Eq. (18) gives that $k_u^t = Y_u^t$ The (apparent) extreme-fiber strain is

$$\varepsilon_{max}^t = \bar{\kappa} z_{max} \qquad (D.2)$$

Substitution and using that $\bar{C}_I^0 \propto h^3$ and $z_{max} \propto h$ gives

$$k_u^t = \frac{\left(\varepsilon_{max}^t\right)^2}{2\left(z_{max}\right)^2} \bar{C}_I^0 \propto h\left(\varepsilon_{max}^t\right)^2. \qquad (D.3)$$

Thus, if k^t is constant with respect to the height h, the apparent

tensile onset strain must scale as

$$\varepsilon_{max}^t(h) \propto h^{-1/2}. \qquad (D.4)$$

This is exactly the same asymptotic size effect as Bažant's classical size-effect law [30]:

$$\varepsilon_0^t(h) = \frac{f_t'}{E} \frac{1}{\sqrt{1 + h/h_a}}, \qquad (D.5)$$

where E is Young's modulus, f_t' the tensile strength in the small-size limit, h_a is the transitional size parameter, directly related to the fracture process zone length, and h the characteristic size of the structure (here taken as the section height). In the case of scale separation, i.e., $h \gg h_a$, this reduces to

$$\varepsilon_0^t(h) \sim \left(\frac{f_t'}{E} \sqrt{h_a} \right) h^{-1/2} \propto h^{-1/2} \qquad (D.6)$$

Appendix E. Parameters used for the fully resolved model

The parameters used for the fully resolved model, i.e., both for the RVE simulations in Section 2.3 and the DNS of the slab in Section 3.3 are presented in Table E.2

Table E.2
Material and bond-slip model parameters used for the fully resolved simulations of TRC.

Parameter	Value	Unit
Concrete matrix		
Tensile Strength, $f_{c,t}$	4.35	MPa
Compressive Strength, $f_{c,c}$	67.8	MPa
Young's Modulus, E_c	40.7	GPa
Poisson's Ratio, v_c	0.200	–
Ultimate Compressive Strain, $\varepsilon_{c,u}$	2.90×10^{-3}	–
Fracture Energy, G_F	156	N m^{-1}
Damage Parameter, A_c	1.16	–
Damage Parameter, B_c	282	–
Compressive Strain Threshold, $\varepsilon_{0,c}$	5.00×10^{-4}	–
Textile yarns		
Nominal Young's Modulus, E_r^0	242	GPa
Nominal Tensile Strength, f_u^0	3.97	GPa
Efficiency Factor for Strength, η_f	0.7	–
Efficiency Factor for Stiffness, η_E	0.7	–
Yarn Area, A_r	5.47	mm^2
Yarn Spacing, s_r	25	mm
Bond-slip interface		
Initial Bond Stress, τ_f	0.822	MPa
Maximum Bond Stress, τ_{max}	2.910	MPa
Shape Parameter, α	0.316	–
Slip Parameter, s_0	0.015	mm
Slip Parameter, s_1	0.025	mm
Slip Parameter, s_2	0.086	mm
Slip Parameter, s_3	1.092	mm

Appendix F. Generalized strain paths used for calibration

Below are the generalized strain paths used for model calibration. They are shown separately for each height, since the RVE simulations were terminated at different load steps, making a common normalization (as in the validation case) impossible (Figs. F.19–F.21).
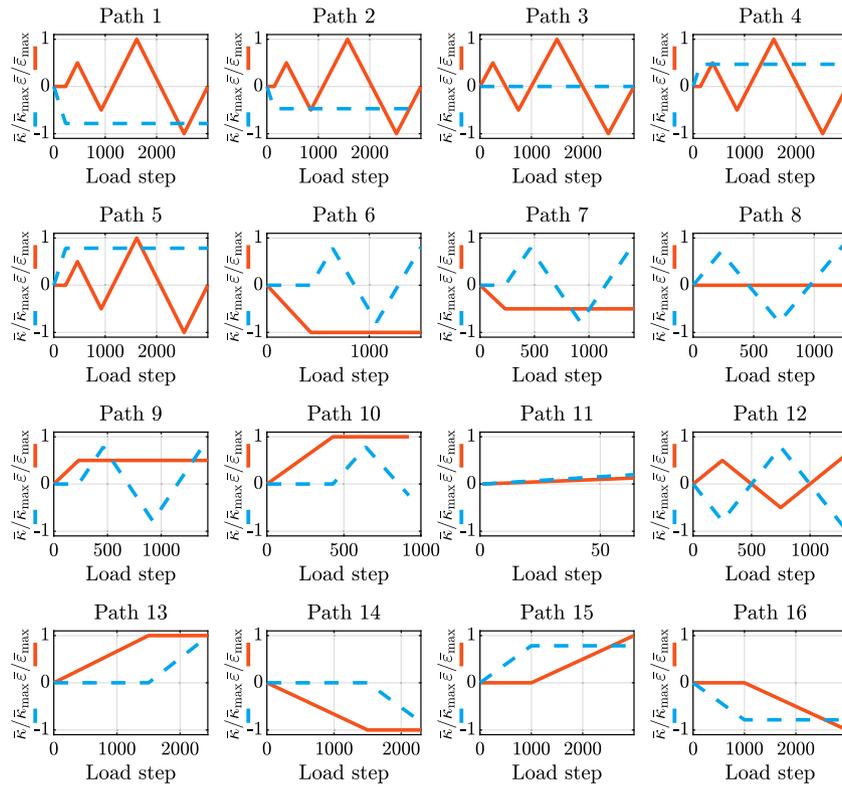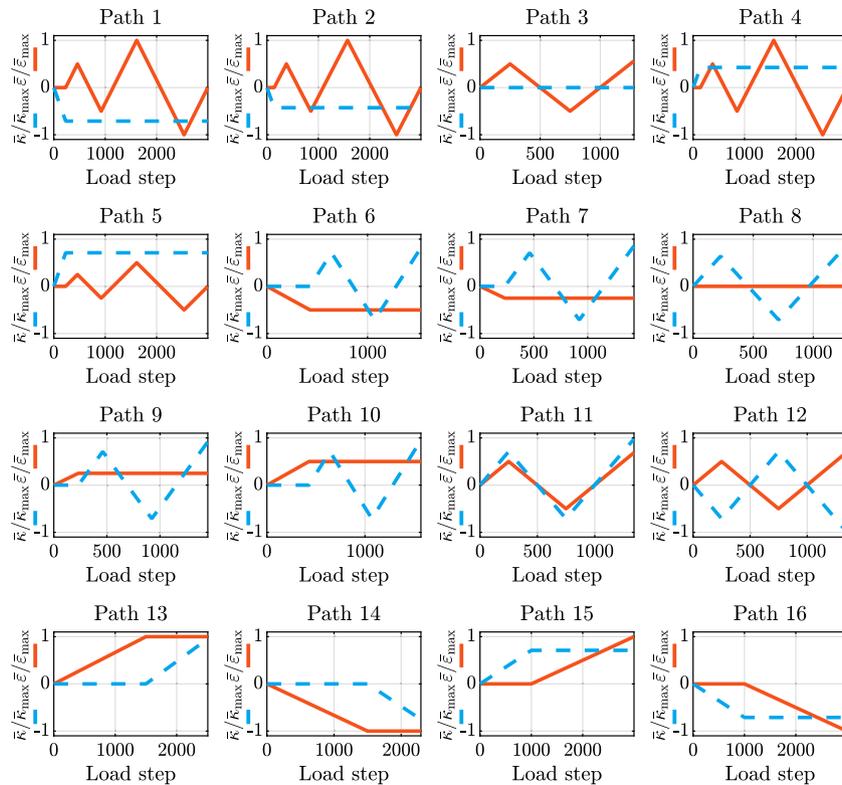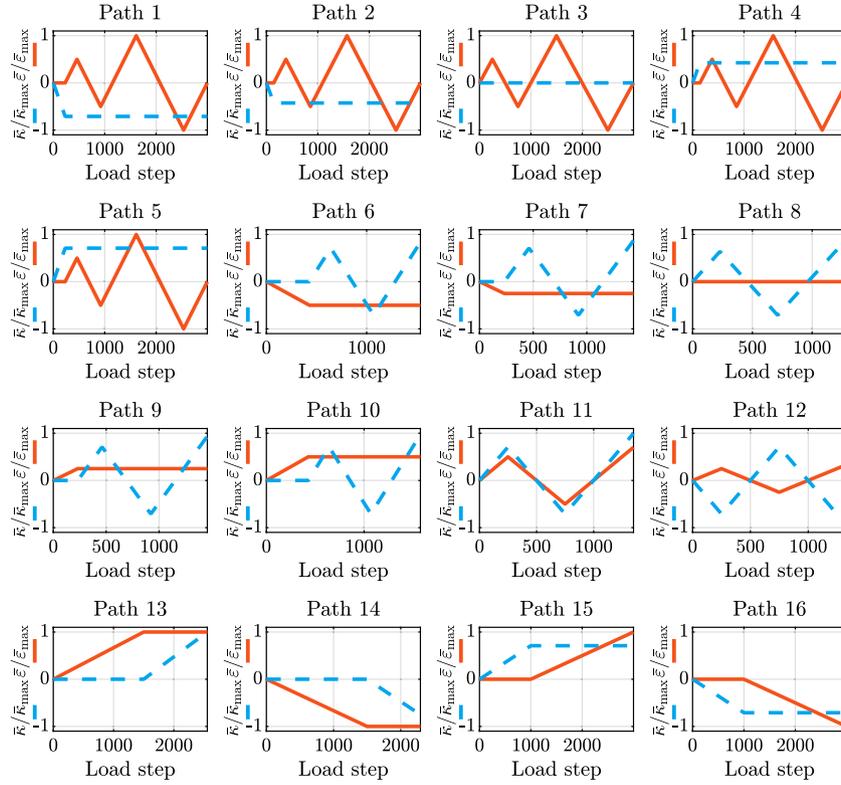

Fig. F.19. Generalized strain paths for $h = 10$ mm used for calibration of the model. $\bar{\varepsilon}$ are normalized by $\bar{\varepsilon}_{\max} = 0.40 \cdot 10^{-3}$, and $\bar{\kappa}$ by $\bar{\kappa}_{\max} = 0.38\,\mathrm{m}^{-1}$.

Fig. F.20. Generalized strain paths for $h = 15$ mm used for calibration of the model. $\bar{\varepsilon}$ are normalized by $\bar{\varepsilon}_{\max} = 0.40 \cdot 10^{-3}$, and $\bar{\kappa}$ by $\bar{\kappa}_{\max} = 0.28\,\mathrm{m}^{-1}$.

Fig. F.21. Generalized strain paths for $h = 20$ mm used for calibration of the model. $\bar{\varepsilon}$ are normalized by $\bar{\varepsilon}_{\max} = 0.40 \cdot 10^{-3}$, and $\bar{\kappa}$ by $\bar{\kappa}_{\max} = 0.21\,\text{m}^{-1}$.

Appendix G. Closed form solutions of sectional moments

The closed-form solutions of the sectional quantities as used in Eq. (28) are displayed in Table G.3. The auxiliary neutral axis are defined as

$$z_{\text{NA,u}} = \begin{cases} \dfrac{\bar{\varepsilon}}{\bar{\kappa}}, & \text{if } \dfrac{\bar{\varepsilon}}{\bar{\kappa}} \geq 0 \text{ and } \left|\dfrac{\bar{\varepsilon}}{\bar{\kappa}}\right| \leq \dfrac{\tilde{h}}{2} \\ 0, & \text{otherwise} \end{cases} \quad z_{\text{NA,l}} = \begin{cases} \dfrac{\bar{\varepsilon}}{\bar{\kappa}}, & \text{if } \dfrac{\bar{\varepsilon}}{\bar{\kappa}} < 0 \text{ and } \left|\dfrac{\bar{\varepsilon}}{\bar{\kappa}}\right| \leq \dfrac{\tilde{h}}{2} \\ 0, & \text{otherwise} \end{cases} \tag{G.1}$$

Table G.3
Closed-form expressions for sectional properties over the four subdomains using splits at the neutral axes $z_{\text{NA,u}}$ and $z_{\text{NA,l}}$.

Integral expression	Closed-form result
$A_1 = \int_{-\tilde{b}/2}^{\tilde{b}/2}\int_{z_{\text{NA,u}}}^{\tilde{h}/2} dz\,dy$	$\tilde{b}\left(\dfrac{\tilde{h}}{2} - z_{\text{NA,u}}\right)$
$A_2 = \int_{-\tilde{b}/2}^{\tilde{b}/2}\int_{0}^{z_{\text{NA,u}}} dz\,dy$	$\tilde{b}\,z_{\text{NA,u}}$
$A_3 = \int_{-\tilde{b}/2}^{\tilde{b}/2}\int_{z_{\text{NA,l}}}^{0} dz\,dy$	$-\tilde{b}\,z_{\text{NA,l}}$
$A_4 = \int_{-\tilde{b}/2}^{\tilde{b}/2}\int_{-\tilde{h}/2}^{z_{\text{NA,l}}} dz\,dy$	$\tilde{b}\left(z_{\text{NA,l}} + \dfrac{\tilde{h}}{2}\right)$
$S_1 = \int_{-\tilde{b}/2}^{\tilde{b}/2}\int_{z_{\text{NA,u}}}^{\tilde{h}/2} z\,dz\,dy$	$\dfrac{\tilde{b}}{2}\left(\left(\dfrac{\tilde{h}}{2}\right)^2 - z_{\text{NA,u}}^2\right)$
$S_2 = \int_{-\tilde{b}/2}^{\tilde{b}/2}\int_{0}^{z_{\text{NA,u}}} z\,dz\,dy$	$\dfrac{\tilde{b}}{2} z_{\text{NA,u}}^2$
$S_3 = \int_{-\tilde{b}/2}^{\tilde{b}/2}\int_{z_{\text{NA,l}}}^{0} z\,dz\,dy$	$-\dfrac{\tilde{b}}{2} z_{\text{NA,l}}^2$
$S_4 = \int_{-\tilde{b}/2}^{\tilde{b}/2}\int_{-\tilde{h}/2}^{z_{\text{NA,l}}} z\,dz\,dy$	$\dfrac{\tilde{b}}{2}\left(z_{\text{NA,l}}^2 - \left(\dfrac{\tilde{h}}{2}\right)^2\right)$
$I_1 = \int_{-\tilde{b}/2}^{\tilde{b}/2}\int_{z_{\text{NA,u}}}^{\tilde{h}/2} z^2\,dz\,dy$	$\dfrac{\tilde{b}}{3}\left(\left(\dfrac{\tilde{h}}{2}\right)^3 - z_{\text{NA,l}}^3\right)$
$I_2 = \int_{-\tilde{b}/2}^{\tilde{b}/2}\int_{0}^{z_{\text{NA,u}}} z^2\,dz\,dy$	$\dfrac{\tilde{b}}{3} z_{\text{NA,u}}^3$
$I_3 = \int_{-\tilde{b}/2}^{\tilde{b}/2}\int_{z_{\text{NA,l}}}^{0} z^2\,dz\,dy$	$-\dfrac{\tilde{b}}{3} z_{\text{NA,l}}^3$
$I_4 = \int_{-\tilde{b}/2}^{\tilde{b}/2}\int_{-\tilde{h}/2}^{z_{\text{NA,l}}} z^2\,dz\,dy$	$\dfrac{\tilde{b}}{3}\left(z_{\text{NA,l}}^3 + \left(\dfrac{\tilde{h}}{2}\right)^3\right)$

Appendix H. Validation results

Below are the results from the validation of the model for generalized strain paths 1, 4, 5, 6 and 8 (Figs. H.22–H.26).
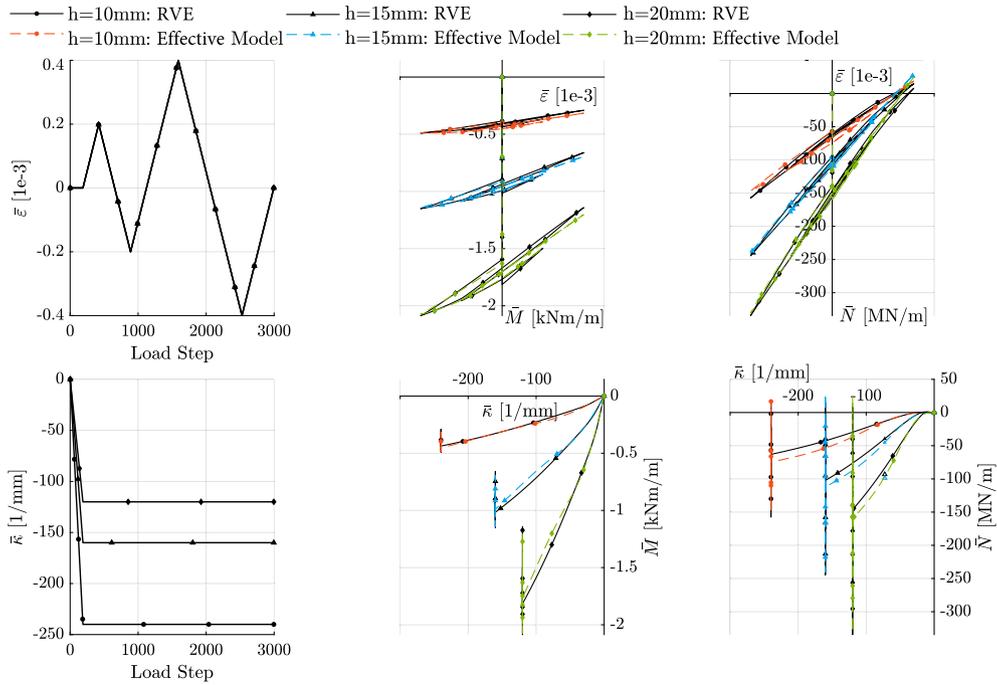

Fig. H.22. Comparison of generalized quantities from effective and RVE model for strain path 1.
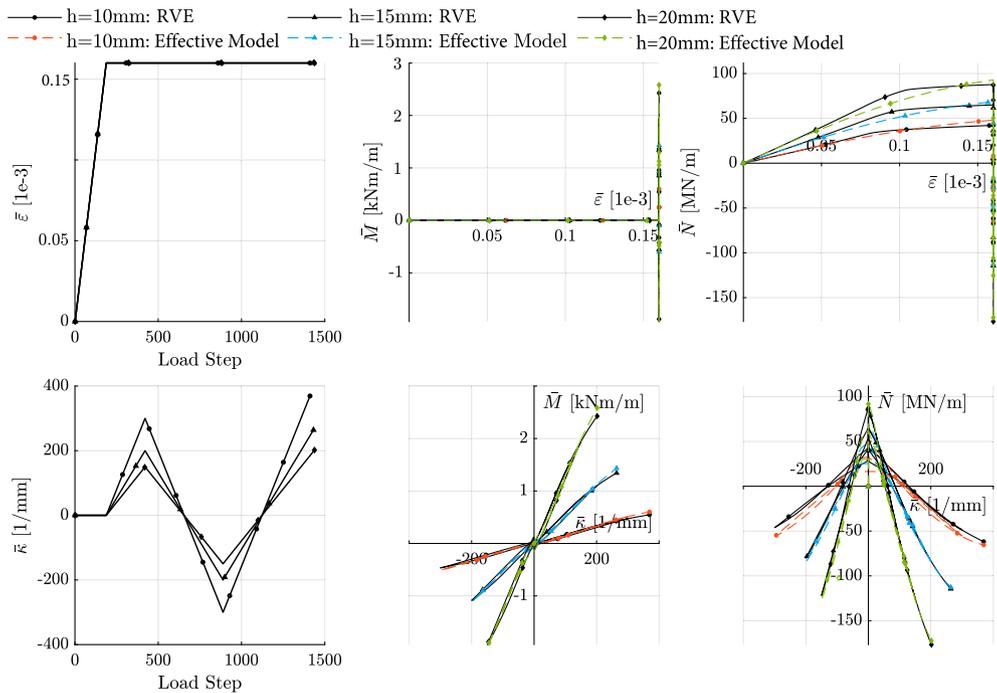

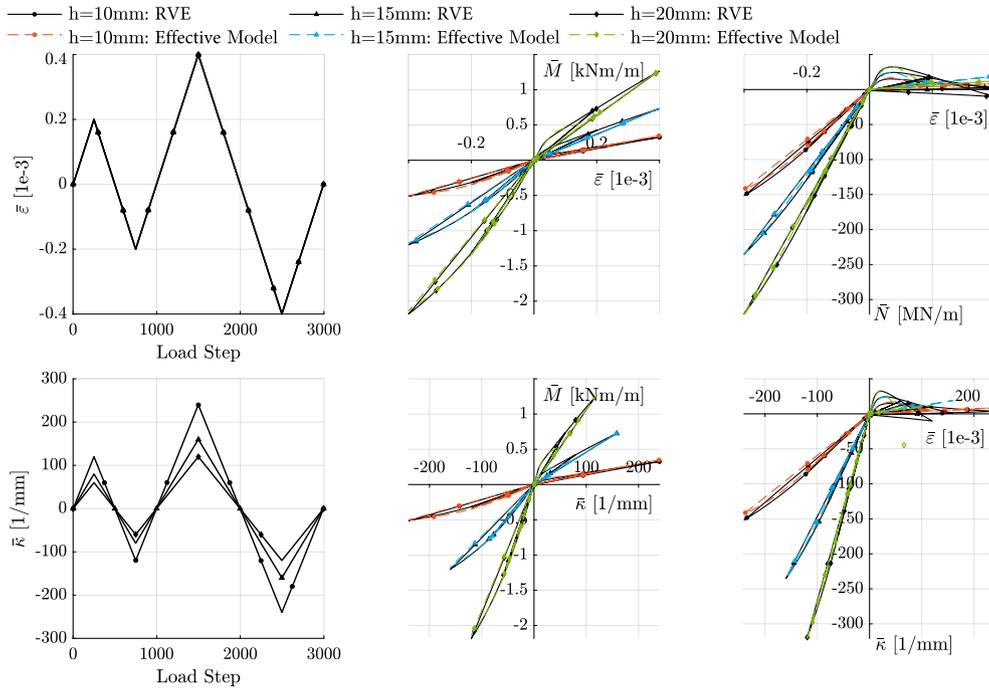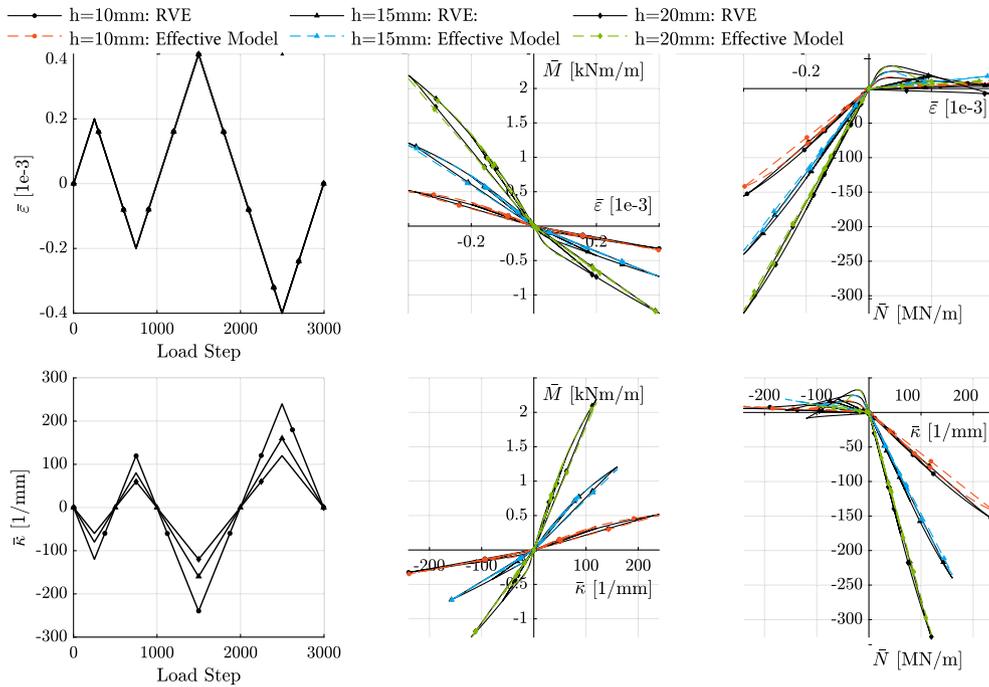**Fig. H.23.** Comparison of generalized quantities from effective and RVE model for strain path 4.

Fig. H.24. Comparison of generalized quantities from effective and RVE model for strain path 5.

Fig. H.25. Comparison of generalized quantities from effective and RVE model for strain path 6.
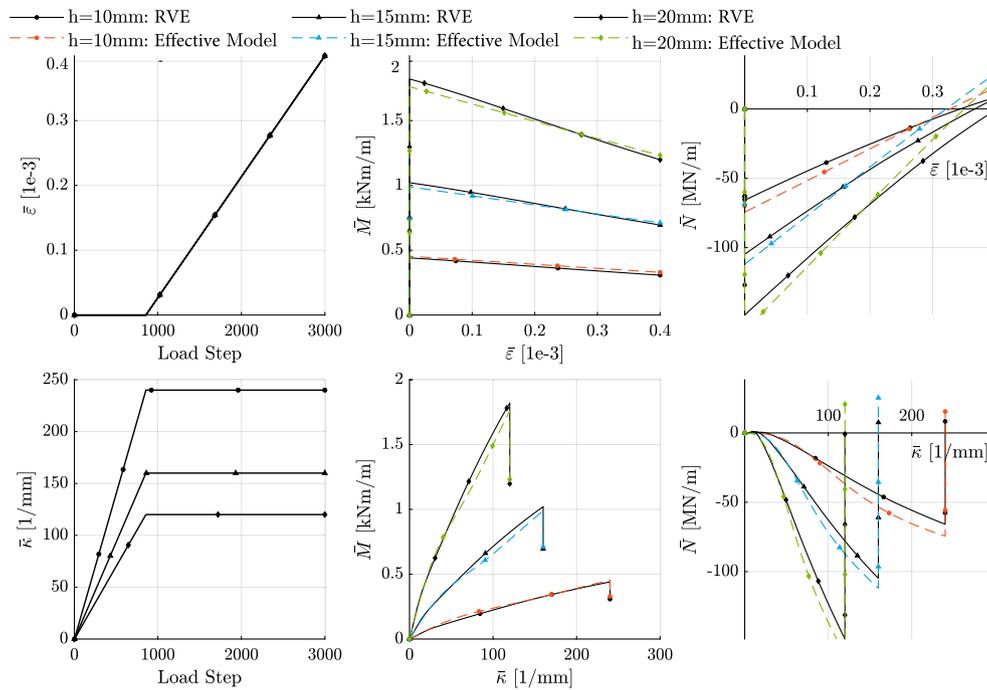
Fig. H.26. Comparison of generalized quantities from effective and RVE model for strain path 8.

Data availability

Data will be made available on request.

References

[1] Fuchs A, Curosu I, Kaliske M. Numerical mesoscale analysis of textile reinforced concrete. Materials 2020;13(18):3944. https://doi.org/10.3390/ma13183944

[2] Holler S, Butenweg C, Noh S-Y, Meskouris K. Computational model of textile-reinforced concrete structures. Comput Struct 2004;82(23):1971–9. https://doi.org/10.1016/j.compstruc.2004.03.076. https://www.sciencedirect.com/science/article/pii/S0045794904002238.

[3] Preinstorfer P, Kromoser B, Kollegger J. Flexural behaviour of filigree slab elements made of carbon reinforced UHPC. Constr Build Mater 2019;199:416–23. https://doi.org/10.1016/j.conbuildmat.2018.12.027

[4] Yu Q, Valeri P, Fernández Ruiz M, Muttoni A. A consistent safety format and design approach for brittle systems and application to textile reinforced concrete structures. Eng Struct 2021;249:113306. https://doi.org/10.1016/j.engstruct.2021.113306

[5] Kadi ME, Tysmans T, Verbruggen S, Vervloet J, De Munck M, Wastiels J, Van Hemelrijck D. A layered-wise, composite modelling approach for fibre textile reinforced cementitious composites. Cem Concr Compos 2018;94:107–15. https://doi.org/10.1016/j.cemconcomp.2018.08.015

[6] Wang J, Ou B, Jia M, Cheng W. Modified microplane model for reinforced concrete under static and dynamic loadings. J Eng Mech 2011;137(10):635–47. https://doi.org/10.1061/(ASCE)EM.1943-7889.0000265

[7] Chudoba R, Sharei E, Scholzen A. A strain-hardening microplane damage model for thin-walled textile-reinforced concrete shells, calibration procedure, and experimental validation. Compos Struct 2016;152:913–28. https://doi.org/10.1016/j.compstruct.2016.06.030

[8] Chudoba R, Sharei E, Senckpiel-Peters T, Schladitz F. Numerical modeling of non-uniformly reinforced carbon concrete lightweight ceiling elements. Appl Sci 2019;9(11):2348. https://doi.org/10.3390/app9112348. https://www.mdpi.com/2076-3417/9/11/2348.

[9] Edefors G, Larsson F, Lundgren K. Computational homogenization for predicting the effective response of planar textile-reinforced concrete shells. Int J Solids Struct 2025;320:113472. https://doi.org/10.1016/j.ijsolstr.2025.113472. https://www.sciencedirect.com/science/article/pii/S0020768325002586.

[10] Dornheim J, Morand L, Nallani HJ, Helm D. Neural networks for constitutive modeling: from universal function approximators to advanced models and the integration of Physics. Arch Comput Methods Eng 2024;31(2):1097–127. https://doi.org/10.1007/s11831-023-10009-y

[11] Balmer VM, Kaufmann W, Kraus MA. Physics-informed neural networks for nonlinear analysis of reinforced concrete beams. In: Lecture notes in civil engineering, vol. 494. Springer Science and Business Media Deutschland GmbH; 2024. p. 271–80. https://doi.org/10.1007/978-3-031-60271-9_24

[12] Schommartz JO, Klein DK, Alzate Cobo JC, Weeger O. Physics-augmented neural networks for constitutive modeling of hyperelastic geometrically exact beams. Comput Methods Appl Mech Eng 2025;435:117592. https://doi.org/10.1016/j.cma.2024.117592. https://www.sciencedirect.com/science/article/pii/S0045782524008466.

[13] Ibrahimbegović A, Frey F. Stress resultant finite element analysis of reinforced concrete plates. Eng Comput 1993;10:15–30. https://doi.org/10.1108/eb023911

[14] Addessi D, Ciampi V. A regularized force-based beam element with a damage–plastic section constitutive law. Int J Numer Methods Eng 2007;70(5):610–29. https://doi.org/10.1002/nme.1911

[15] Koechlin P, Potapov S. Global constitutive model for reinforced concrete plates. J Eng Mech 2007;133(3):257–66. https://doi.org/10.1061/(ASCE)0733-9399(2007)133:3(257).

[16] Markovic D, Koechlin P, Voldoire F. Reinforced concrete structures under extreme loading: stress resultant global reinforced concrete models (glrc). In: Papadrakakis M, Charmpis DC, Lagaros ND, Tsompanakis Y, editors. Proceedings of the ECCOMAS thematic conference on computational methods in structural dynamics and earthquake Engineering (COMPDYN 2007). Rethymno, Crete, Greece; 2007.

[17] Huguet M, Erlicher S, Kotronis P, Voldoire F. Stress resultant nonlinear constitutive model for cracked reinforced concrete panels. Eng Fract Mech 2017;176:375–405. https://doi.org/10.1016/j.engfracmech.2017.02.027

[18] Sciegaj A, Almfeldt S, Larsson F, Lundgren K. Textile reinforced concrete members subjected to tension, bending, and in-plane loads: experimental study and numerical analyses. Constr Build Mater 2023;408. https://doi.org/10.1016/j.conbuildmat.2023.133762

[19] Save MA, Massonnet CE, de Saxce G. 5. Generalized variables. In: North-Holland series in applied mathematics and mechanics, vol. 43. North-Holland; 1997. p. 83–147. https://doi.org/10.1016/S0167-5931(97)80022-8. https://www.sciencedirect.com/science/article/pii/S0167593197800228.

[20] Ottosen N, Petersson H. Introduction to the finite element method. Prentice-Hall; 1992.

[21] Marigo J-J. Modelling of brittle and fatigue damage for elastic material by growth of microvoids. Eng Fracture Mech 1985;21:861–74. https://doi.org/10.1016/0013-7944(85)90093-1

[22] Mazars J. A description of micro- and macroscale damage of concrete structures. Eng Fract Mech 1986;25:729–37.

[23] Meyer KA, Ekre F. Thermodynamically consistent neural network plasticity modeling and discovery of evolution laws. J Mech Phys Solids 2023;180. https://doi.org/10.1016/j.jmps.2023.105416

[24] Lubarda VA. On the gibbs conditions of stable equilibrium, convexity and the second-order variations of thermodynamic potentials in nonlinear thermoelasticity. Int J Solids Struct 2008;45:48–63. https://doi.org/10.1016/j.ijsolstr.2007.07.010

[25] Jirásek M. Damage and smeared crack models. In Pijaudier-Cabot G, Grassl P, La Borderie C, editors. Numerical modeling of concrete cracking. Springer; 2011. p. 1–49. https://doi.org/10.1007/978-3-7091-0897-0_1

[26] Mazars J, Hamon F, Grange S. A new 3d damage model for concrete under monotonic, cyclic and dynamic loadings. Mater Struct 2015;48(11):3779–93. https://doi.org/10.1617/s11527-014-0439-8. https://hal.science/hal-01753975.

[27] Bažant ZP, Oh BH. Crack band theory for fracture of concrete. Materiaux Constr 1983;16:155–77. https://doi.org/10.1007/BF02486267

[28] Sciegaj A, Larsson F, Lundgren K. Experiments and calibration of a bond-slip relation and efficiency factors for textile reinforcement in concrete. Cem Concr Compos 2022;134:104756. https://doi.org/10.1016/j.cemconcomp.2022.104756

[29] Richter M. Development of mechanical models for the analytical description of the material behaviour of textile reinforced concrete [Ph.D. thesis]. TU Dresden; 2005. https://nbn-resolving.org/urn:nbn:de:swb:14-1124353924615-82806.

[30] Bažant ZP. Size effect in blunt fracture: concrete, rock, metal. J Eng Mech 1984;110(4):518–35. https://doi.org/10.1061/(ASCE)0733-9399(1984)110:4(518)

[31] Mobasher B. Textile fiber composites: testing and mechanical behavior. In Triantafillou T, editor. Textile fibre composites in civil engineering. Woodhead Publishing; 2016. p. 101–50. https://doi.org/10.1016/B978-1-78242-446-8.00006-9. https://www.sciencedirect.com/science/article/pii/B9781782424468000069.

[32] Hartig J, Häußler-Combe U, Schicktanz K. Influence of bond properties on the tensile behaviour of textile reinforced concrete. Cem Concr Compos 2008;30(10):898–906. https://doi.org/10.1016/j.cemconcomp.2008.08.004. https://www.sciencedirect.com/science/article/pii/S0958946508001121.

[33] Rampini MC, Zani G, Colombo M, Di Prisco M. Stiffness degradation of textile-reinforced mortar under unloading–reloading tensile cycles. J Compos Constr 2023;27(1):04022083. https://doi.org/10.1061/(ASCE)CC.1943-5614.0001273. https://ascelibrary.org/doi/10.1061/(ASCE)CC.1943-5614.0001273.

[34] Hartig J, Häußler-Combe U, Schicktanz K. A lattice model approach to the uniaxial behaviour of textile reinforced concrete. In: Carpinteri A, Gambarova PG, Ferro G, Plizzari GA, editors. Proceedings of the 6th International Conference on fracture Mechanics of concrete and concrete structures (Framcos-6). Catania, Italy: Taylor & Francis; 2007. p. 745–52.

[35] Hartig JU. Numerical investigations on the uniaxial tensile behaviour of textile reinforced concrete numerische untersuchungen zum einaxialen zugtragverhalten von textilbeton [Ph.D. thesis]. Technische Universität Dresden. Aug 2010.

[36] Grassl P, Jirásek M. Damage-plastic model for concrete failure. Int J Solids Struct 2006;43(22):7166–96. https://doi.org/10.1016/j.ijsolstr.2006.06.032. https://www.sciencedirect.com/science/article/pii/S002076830600240X.

[37] Grassl P, Xenos D, Nyström U, Rempling R, Gylltoft K. Cdpm2: a damage-plasticity approach to modelling the failure of concrete. Int J Solids Struct 2013;50(24):3805–16. https://doi.org/10.1016/j.ijsolstr.2013.07.008. https://www.sciencedirect.com/science/article/pii/S0020768313002886.